

Research Article: New Research | Disorders of the Nervous System

## Neonatal Brain Injury Triggers Niche-Specific Changes to Cellular Biogeography

<https://doi.org/10.1523/ENEURO.0224-24.2024>

Received: 28 May 2024

Revised: 28 October 2024

Accepted: 18 November 2024

Copyright © 2024 Tahmasian et al.

This is an open-access article distributed under the terms of the [Creative Commons Attribution 4.0 International license](#), which permits unrestricted use, distribution and reproduction in any medium provided that the original work is properly attributed.

---

*This Early Release article has been peer reviewed and accepted, but has not been through the composition and copyediting processes. The final version may differ slightly in style or formatting and will contain links to any extended data.*

**Alerts:** Sign up at [www.eneuro.org/alerts](http://www.eneuro.org/alerts) to receive customized email alerts when the fully formatted version of this article is published.

**1. Manuscript Title:** Neonatal Brain Injury Triggers Niche-Specific Changes to Cellular Biogeography

**2. Abbreviated Title:** Spatial transcriptomics in mouse model of preterm brain injury

**3. Author Names and Affiliations:**

Nareh Tahmasian<sup>1,2,3,12</sup>, Min Yi Feng<sup>1,4,12</sup>, Keon Arbabi<sup>5,6,12</sup>, Bianca Rusu<sup>1,4</sup>, Wuxinhao Cao<sup>1</sup>, Bharti Kukreja<sup>1</sup>, Asael Lubotzky<sup>7</sup>, Michael Wainberg<sup>6,8,9</sup>, Shreejoy J. Tripathy<sup>5,6,8,10,\*</sup>, Brian T. Kalish<sup>1,4,11\*</sup>

1. Program in Neuroscience and Mental Health, SickKids Research Institute, Toronto, ON M5G 1L7, Canada
2. Department of Laboratory Medicine and Pathology, University of Toronto, Toronto, ON M5S 1A8, Canada
3. Department of Biological Sciences, Sunnybrook Research Institute, Toronto, ON M4N 3M5, Canada
4. Department of Molecular Genetics, University of Toronto, Toronto, ON M5G 1A8, Canada
5. Institute of Medical Science, University of Toronto, Toronto, ON M5G 1A8, Canada
6. Krembil Centre for Neuroinformatics, Centre for Addiction and Mental Health, Toronto, ON M5T 1R8, Canada
7. Division of Neurology, Department of Paediatrics, Hospital for Sick Children, Toronto, ON M5G 1L7, Canada
8. Department of Psychiatry, University of Toronto, Toronto, ON M5G 1A8, Canada.
9. Prosserman Centre for Population Health Research, Lunenfeld-Tanenbaum Research Institute, Sinai Health, Toronto, ON M5G 1X5, Canada
10. Department of Physiology, University of Toronto, Toronto, ON M5G 1A8, Canada
11. Division of Neonatology, Department of Paediatrics, Hospital for Sick Children, Toronto, ON M5G 1L7, Canada
12. These authors contributed equally to this work.

**4. Author Contributions:** Overall conceptualization, B.T.K. and S.J.T.; tissue acquisition and processing, B.T.K. and N.T.; MERFISH sample preparation and imaging, N.T.; computational data analysis, N.T., M.Y.F., K.A., R.X., B.K., M.W., S.J.T., and B.R.; manuscript preparation and writing, B.T.K., N.T., M.Y.F., K.A., S.J.T., A.L., and B.R.; figure design and preparation, B.R., and N.T.; funding acquisition, B.T.K.; supervision and project administration, B.T.K.

**5. Correspondence should be Addressed to:** Brian T. Kalish at [brian.kalish@sickkids.ca](mailto:brian.kalish@sickkids.ca).

**6. Number of Figures:** 7

**7. Number of Tables:** 0

**8. Number of Multimedia:** 0

**9. Number of Words for Abstract:** 144

**10. Number of Words for Significance Statement:** 105

**11. Number of Words for Introduction:** 622

**12. Number of Words for Discussion:** 1295

**13. Acknowledgements:** None

**14. Conflict of Interest:** The authors report no conflict of interest.

**15. Funding Sources:** This study was funded by a Brain Canada Future Leaders in Canadian Neuroscience award to BTK. The funders had no role in study design, data collection and interpretation, or the decision to submit the work for publication.

9 **ABSTRACT**

10 Preterm infants are at risk for brain injury and neurodevelopmental impairment due, in part, to white  
11 matter injury following chronic hypoxia exposure. However, the precise molecular mechanisms by which  
12 neonatal hypoxia disrupts early neurodevelopment are poorly understood. Here, we constructed a brain-  
13 wide map of the regenerative response to newborn brain injury using high-resolution imaging-based  
14 spatial transcriptomics to analyze over 800,000 cells in a mouse model of chronic neonatal hypoxia.  
15 Additionally, we developed a new method for inferring condition-associated differences in cell type spatial  
16 proximity, enabling the identification of niche-specific changes in cellular architecture. We observed  
17 hypoxia-associated changes in region-specific cell states, cell type composition, and spatial organization.  
18 Importantly, our analysis revealed mechanisms underlying reparative neurogenesis and gliogenesis,  
19 while also nominating pathways that may impede circuit rewiring following neonatal hypoxia. Altogether,  
20 our work provides a comprehensive description of the molecular response to newborn brain injury.

32  
33  
34  
35  
36  
37  
38  
39  
40  
41  
42  
43  
44  
45  
46  
47  
48  
49  
50  
51  
52  
53  
54

## **SIGNIFICANCE STATEMENT**

Children born prematurely are at risk for white matter injury and cerebral dysmaturation, which predispose to life-long neurological impairments. Here, we used a mouse model of chronic neonatal hypoxia that mimics some of the features of preterm brain injury and performed high resolution spatial transcriptomics using multiplexed error-robust fluorescence *in situ* hybridization (MERFISH). We developed a new approach to map cell-cell relationships, which revealed profound changes to cellular organization in response to newborn brain injury. We defined cellular communication networks and signaling pathways that likely contribute to hypoxia-responsive neurogenesis and gliogenesis, as well as cell- and region-specific factors that may disrupt neurologic recovery and repair.

## 59 **INTRODUCTION**

60 Preterm birth is the leading cause of neonatal morbidity and mortality in developed countries and  
61 affects approximately 15 million infants annually (Blencowe et al., 2013a). While significant strides have  
62 been made in neonatal health care leading to increased survival rates, the long-term impact of premature  
63 birth on the trajectory of neurodevelopment remains a major unsolved challenge. Survivors of preterm  
64 birth are at high risk for neurodevelopmental impairment, including cognitive and motor disability, as well  
65 as autism spectrum disorder, epilepsy, and attention-deficit/hyperactivity disorder (Blencowe et al.,  
66 2013b; Crump et al., 2021; Hirvonen et al., 2017; Rommel et al., 2017). The causes of brain injury in  
67 preterm infants are complex and multifactorial, but chronic exposure to hypoxia (HX) due to lung  
68 immaturity is an important driver of brain injury and maldevelopment. Importantly, white matter injury  
69 (WMI) is most prevalent in infants born at early gestational ages preceding the onset of myelination. This  
70 suggests a developmental susceptibility of immature oligodendrocyte (OL)-lineage cells to HX-ischemia,  
71 oxidative stress, and impaired cerebral perfusion, leading to maturational failure (Salmaso et al., 2014).  
72 Despite this understanding, we lack therapies to protect the preterm brain or to promote recovery during  
73 this critical developmental window.

74 A mouse model of chronic sublethal HX, in which neonatal mice are exposed to one week of 10%  
75 oxygen, replicates many structural and pathophysiological aspects of human preterm injury and has been  
76 widely used to study preterm WMI (Fagel et al., 2006; Forbes et al., 2020; Jablonska et al., 2022;  
77 Salmaso et al., 2014). However, most studies have focused on injury and repair within the OL-lineage,  
78 rather than brain-wide changes in the response to neonatal HX and the role of cell-cell communication  
79 networks. Importantly, there is growing recognition that the local microenvironment in specific brain  
80 regions dictates many aspects of cell fate and state (Herrero-Navarro et al., 2021; Joglekar et al., 2021;  
81 Tan et al., 2020), which highlights the necessity of characterizing brain region-specific cellular programs  
82 that govern recovery and repair. Glial identity varies based on cortical location (Hilscher et al., 2022;  
83 Spitzer et al., 2019; Stogsdill et al., 2022) and the local spatial niche may inform injury response (Brandi  
84 et al., 2022; Hammond et al., 2019). It is therefore likely, but incompletely understood, that a similar  
85 region-specific injury response occurs in the context of chronic neonatal HX.

86 To address this gap in knowledge, we applied spatially resolved single-cell transcriptomics  
87 (multiplexed error-robust fluorescence *in situ* hybridization, MERFISH) to explore how neonatal HX  
88 affects the brain's spatial organization and signaling landscape. Unlike traditional droplet-based single-  
89 cell genomics, MERFISH captures sub-cellular localization of gene expression within the native tissue  
90 context, offering insight into cellular organization and architecture (Allen et al., 2023; Zhang et al., 2023,  
91 2021). We performed MERFISH on the mouse brain following chronic sublethal neonatal HX and on age-  
92 matched normal oxygen (normoxic, NX) controls. At baseline (under NX conditions), we identified brain  
93 region-specific cell states and signaling-associated gene expression profiles in non-neuronal cells.  
94 Following neonatal HX, we identified increased oligodendrocyte precursor cell (OPC) proliferation but  
95 arrested differentiation of these cells into mature OL in the subventricular zone (SVZ) and corpus  
96 callosum. We characterized region- and cell type-specific gene expression changes that may inhibit  
97 functional myelination and repair, including upregulation of extracellular matrix components and other  
98 mediators known to inhibit oligodendrogenesis. Further, to quantify compositional changes to the cellular  
99 microenvironment after HX, we developed a novel approach to infer changes in the spatial proximity of  
100 neighboring cell types. Using this method, we found extensive reorganization of local cellular architecture  
101 in the cortex, SVZ, and corpus callosum following HX. Overall, these results provide novel insights into  
102 the mechanisms underlying white matter regeneration in the neonatal brain and underscore the complex  
103 multicellular processes in the regenerative response to HX-induced preterm WMI.

104

## 105 **MATERIALS AND METHODS**

### 106 **Mouse Model of Chronic Sublethal Hypoxia**

107 All animal experiments were performed in accordance with the SickKids Research Institute  
108 policies. CD-1 mice (Strain: 022) were purchased from Charles River Laboratories. The animals were  
109 kept in 12/12 hour light/dark cycles with free access to food and chow, and bred at the [AUTHOR'S  
110 UNIVERSITY]. Offspring CD-1 mice were exposed to an oxygen concentration of either 10% (HX) or  
111 21% (NX) in a HX chamber from postnatal day 3 (P3) to P11, lasting eight consecutive days (Fagel et al.,

2006; Jablonska et al., 2022; Sathyanesan et al., 2018). Mouse dams were rotated daily. At P11, mice were removed from the chamber and transferred to a room with normoxic conditions (21% oxygen) until euthanasia by CO<sub>2</sub> at P21. Fresh brain tissue was harvested and immediately placed in optimal cutting temperature (OCT) solution and frozen at -80°C until MERFISH processing. Male offspring were used for MERFISH experiments.

**MERFISH Gene Panel Design**

We created a panel of 497 genes (Extended Data Table 1-1) to study the cellular architecture and signaling landscape of the murine forebrain using MERFISH. To guide the identification of diverse cell types in the brain, the panel included 181 genes that are known cell-type specific markers or have been previously shown to have enriched expression in a specific population of cells. This list targeted known cell types within major forebrain structures including the cortex, white matter tracts, striatum, and SVZ. The remaining 316 genes were components of biological pathways shown previously or hypothesized to play a role in the pathophysiology of chronic neonatal HX. This included components of signaling pathways known to regulate oligodendrogenesis, myelination, or that have previously been implicated in the pathophysiology of WMI such as WNT signaling (Chavali et al., 2020; Varela-Nallar et al., 2014), BMP signaling (Dizon et al., 2011; Wu et al., 2012), SHH signaling (Bergles and Richardson, 2015; Wu et al., 2012), FGF signaling (Furusho et al., 2015, 2012), EGF signaling (Aguirre et al., 2007), Ephrin signaling (Harboe et al., 2018; Li et al., 2022), cytokine signaling (Kirby et al., 2019), senescence (Nicaise et al., 2019; Safaiyan et al., 2016), and oncogenes (Courtois-Cox et al., 2008). Each gene was assigned a 20-bit binary barcode which was used to decode sequential imaging data to assign detected transcripts to the appropriate gene.

**MERFISH Tissue Processing and Sample Preparation**

All MERFISH sample preparation was performed under RNase-free conditions. Frozen embedded brains were cryo-sectioned at 10 µm thickness at -21°C and mounted onto room temperature (RT) MERSCOPE beaded coverslips (Vizgen, Cat: 10500001). After adhering, sections were allowed to refreeze for 5-15 min, then fixed in 4% paraformaldehyde (PFA) diluted in 1X PBS for 15 min. Sections

138 were washed three times with 1X PBS for 5 min each, then stored in 70% ethanol (EtOH) overnight at  
139 4°C to permeabilize the tissue. Sections were stored in 70% EtOH for a maximum of 3 weeks.

140 Sample preparation was performed using the sample preparation kit (Vizgen, Cat: 10400012) and  
141 Vizgen manufacturer instructions for unfixed tissue. First, sections were washed with 1X PBS followed by  
142 Sample Prep Wash Buffer (Vizgen, PN 20300001). Sections were incubated in Formamide Wash Buffer  
143 (Vizgen, PN 20300002) for 30 min at 37°C, then incubated in the gene panel mix for 42-46 hour (hr) at  
144 37°C. Sections were then incubated two times in Formamide Wash Buffer for 30 min each at 47°C, and  
145 washed with sample prep wash buffer for at least 2 min. Sections were coated in gel embedding solution  
146 (0.05% w/v ammonium persulfate, 0.05% v/v N,N,N',N'-tetramethylethylenediamine in Gel Embedding  
147 Premix (Vizgen, PN 20300004)) and incubated at room temperature (RT) for 1.5 hr, cleared in 1:100  
148 proteinase K in Clearing Premix (Vizgen, PN 20300003) at 37°C overnight or for a maximum of 7 days to  
149 clear lipids and proteins that may contribute to auto-fluorescence background noise. Prior to imaging,  
150 sections were washed two times with Sample Prep Wash Buffer, incubated in DAPI and PolyT Staining  
151 Reagent (Vizgen, PN 20300021) for 15 min on a rocking platform, incubated in Formamide Wash Buffer  
152 for 10 min and washed again with Sample Prep Wash Buffer.

153 **MERFISH Imaging**

154 Imaging was performed on the MERSCOPE platform (Vizgen, Cat: 10000001) according to  
155 manufacturer instructions. Briefly, samples were loaded into the flow chamber of the instrument and the  
156 desired region for imaging was selected using a low-resolution mosaic of DAPI and PolyT stains.  
157 Samples were imaged at high-resolution with a 7-plane z-stack and 1.5 µm spacing between adjacent z-  
158 planes to capture the entire 10 µm thickness of the tissue sections. Samples were then automatically  
159 imaged according to MERSCOPE imaging presets.

160 **MERFISH Bioinformatics Workflow**

161 After imaging, transcript barcodes were decoded and assigned to the appropriate gene.  
162 MERFISH images were segmented using Vizgen's post-processing tool (VPT) and Cellpose 2.0  
163 (Pachitariu and Stringer, 2022), a machine learning algorithm (RRID:[SCR\\_021716](#)). DAPI and PolyT



signals were used to delineate cell boundaries for each field-of-view. Individual RNA molecules were assigned to a cell based on whether they were positioned within the marked boundary. Anatomical segmentation was performed based on tissue morphology and region-specific gene expression patterns. This revealed 8 gross anatomical regions: cortex (marked by high expression of *Slc7a6* and *Slc17a7*); corpus callosum, anterior commissure, septal white matter tracts (all marked by high expression of *Cnp* and *Plp1*), SVZ (marked by high expression of *Foxj1*, *Sox2*, and *Asc11*), caudoputamen (marked by high expression of *Foxo1*, *Crym*, and *Gad1/2*), lateral septal nucleus (marked by expression of *Sp8* and *Sp9*), anterior commissure (marked by high expression of *Cnp*, and *Plp1*), bed nucleus of the stria terminalis (marked by *Cartpt*), and the regions ventral to the caudoputamen and anterior commissure, which were collectively labeled lower gray matter (high expression of *Gad1*, and *Dlx1/2*). Meninges (high expression of *Col1a1* and *Gfap*) were grouped with the cortex. The cortex was further segmented into upper, superficial cortex layers (marked by high expression of *Cux2*, *Cartpt*, *Kitl*, and *Rgs8*), and deeper cortex layers (marked by high expression of *Bcl11b*, *Fezf2*, *Otx1*, and *Tle4*).

To obtain a cell-by-gene matrix of each biological sample tissue replicate, we adapted an existing bioinformatic pipeline (Allen et al., 2023) as follows. (1) To remove segmentation artifacts of extremely small or large cells, we removed cells with a volume less than 50 $\mu\text{m}^3$  or larger than three times the median volume of all cells. (2) Cells with zero RNA molecules were removed. (3) In a 10 $\mu\text{m}^2$  thick tissue slice, the spatial orientation of cells within the section resulted in partial imaging of their soma. To account for potential RNA discrepancies, gene expression for each cell was normalized by their volume and multiplied by 1000. (4) Cells with total RNA counts falling below 2% quantile or exceeding the 98% quantile were excluded. (5) Potential doublets were removed using Scrublet (RRID:[SCR\\_018098](#)), a program that generates artificial doublets by comparing gene expression profiles of randomly selecting cells with segmented cells in the dataset and using a k-nearest neighbor (kNN) to output a predicted doublet score. Cells with a Scrublet-based doublet score of greater than 0.20 were excluded for further analysis, accounting for 2.5-3.5% of cells across samples.

Data was then processed using the Seurat V5 package in R (RRID:[SCR\\_016341](#)). First, each dataset was normalized using Seurat's SCTransform function and cells from each gross anatomical

191 region were grouped into separate Seurat objects. We focused subsequent analyses on cells contained  
192 in 3 brain regions: cortex, corpus callosum, and SVZ. We integrated and scaled gene expression from  
193 cells from each of six samples ( $n = 3$  HX and  $n = 3$  NX). Only genes with sufficient expression across  
194 cells in that region (ranging from 475-495 genes) were integrated and used to compute principal  
195 components and uniform manifold approximation and projection (UMAP). Cell clustering was performed  
196 using shared nearest neighbors-clique (SNN-clique). Cell typing and subtyping was performed using canonical  
197 markers. To improve our cell type identification, we removed (1) clusters that did not express cell type-  
198 specific marker genes, and thus could not be assigned to a cell type, and (2) clusters of cells that  
199 expressed two or more mutually exclusive cell-type-specific marker genes. The former excluded potential  
200 non-cell artifacts or cells which could not be identified with the implemented gene panel, and the latter  
201 excluded potential doublets.

## 202 **Cell Proportion Analysis**

203 To determine differences in Cell Type abundance in response to HX, we calculated cell type  
204 proportions for each Cell Subtype class within each region. For each biological replicate and each region,  
205 the total number of cells in each Cell Subtype was divided by either the total number of cells in the region  
206 or the total number of cells in the region corresponding to a broad cell class (e.g., neurons, glia, OL-  
207 lineage). Statistical differences in cell proportions were calculated using an unpaired, two-tailed,  
208 Student's t-test comparing HX and NX ( $n = 3$  each) for each Cell Subtype of each region.

## 209 **Cell-Level Proximity Analysis**

210 To understand how the composition of cellular neighborhoods are affected by neonatal HX, we  
211 developed a novel method to quantify condition-related differences in local cell type proximity. For each  
212 cell  $i$ , a k-dimensional tree was used to count the number of neighboring type B cells,  $N_B$ , and the total  
213 number of neighboring cells (irrespective of type),  $N_{total}$ , within a specified radius  $r$ . For each sample and  
214 brain region, we defined a minimum distance unit,  $d$ , as the median of the smallest distances between all  
215 cell pairs for each sample. A restricted radius ( $r = 5 * d$ ) was selected to focus on the immediate proximity  
216 interactions between Cell Types. The proportion of type B cells within this radius is given by:

$$B_{ratio_i} = \frac{N_B}{N_{total}}$$

The  $B_{ratio}$  provides a normalized measure of the local proportion or density of cell type B in the proximity to a reference cell  $i$ . We note that  $B_{ratio}$  is asymmetric (e.g., the proportion of astrocytes in the proximity of neurons is different from the proportion of neurons in the proximity of astrocytes), which allows for discriminating when the neighborhood of one cell type is enriched or depleted for another cell type, but not vice versa. We further note that this analysis of local cell proximity or density is conceptually similar to the analysis of global cell proportion differences defined above.

To identify differences in local cell type proximity under NX and HX conditions, we used a Generalized Linear Mixed-Effects Model (GLMM) implemented via the glmmTMB R package and goodness-of-fit calculations evaluated by the DHARMA package (RRID:SCR\_022136). This statistical model addresses the non-independence of within-tissue sample observations and is applied to the log-transformed  $B_{ratio}$ , with a small offset to accommodate zeroes. This approach quantifies the impact of condition on cell type distributions, while accounting for inter-sample variability:

$$\log(B_{ratio} + 0.001) \sim Condition + (1|Sample)$$

The effect size and FDR for the condition coefficient were assessed. Significant coefficients (FDR < 0.05) indicated a change in cell proximity under HX conditions relative to NX, suggesting a disruption in cellular neighborhoods. A positive effect size indicated that cell type B is more densely clustered near cell type A (center cell) in HX compared to NX, suggesting increased proximity. In contrast, a negative effect size indicated that cell type B is closer to cell type A in NX compared to HX, indicating a relative decrease in proximity under hypoxic conditions.

### **Differential Gene Expression Analysis**

To identify the differentially expressed genes between conditions and regions, we employed MAST (Finak et al., 2015) using Seurat's FindMarkers function on the raw counts matrix. Only genes expressed in a minimum of 5% of cells in either comparison group were tested. P-values were adjusted with the Benjamini-Hochberg (BH) correction method to obtain FDR values. Specific  $\log_2(FC)$  values are

242 reported in Extended Data Table 5-1. Genes with a  $|\log_2(\text{FC})| > 0.25$  and  $\text{FDR} < 0.05$  were considered  
243 significantly differentially expressed.

244 **Cell State Scoring**

245 To calculate cell state scores, we selected genes whose expression has been previously shown  
246 to be enriched in cells primed for OL differentiation (OL genesis score) or enriched in mature OLs (OL  
247 maturation score (Floriddia et al., 2020; Marques et al., 2016; Takeuchi et al., 2020); enriched in reactive  
248 astrocytes over homeostatic astrocytes (reactive astrocyte score (Liddel et al., 2017; Matusova et al.,  
249 2023; Zamanian et al., 2012)); and enriched in reactive microglia compared to homeostatic microglia  
250 (reactive microglia score) (Paolicelli et al., 2022). Cell state scores were calculated for each cell from the  
251 normalized, integrated datasets by taking the average z-score for the genes in the cell state gene list in  
252 each cell. Then, cell state scores for specific cell groups (i.e., specific Cell Types or Cell Subtypes for  
253 each replicate for each anatomical region) were calculated by taking the average cell state score across  
254 all cells within that group of cells. To compare changes from NX to HX, statistical analysis was performed  
255 using the two-tailed, unpaired, Student's t-test comparing the cell state scores from the 3 NX replicates to  
256 3 HX replicates within each cell type and anatomical region analyzed. Genes used for the OL genesis  
257 score were *Ptprz1*, *Qk*, *Itpr2*, *Gpr17*, *Fyn*, and *Tcf7l2*. Genes used for the OL maturation score were *Mog*,  
258 *Mag*, *Cnp*, *Plp1*, *Myrf*, *Egr2*, *Fos*, *Fosb*, *Klk6*, *Ptgds*, *Car2*, *Grm3*, *Npsr1*, *Jph4*, *Aspa*, *Msmo1*, *Sqle*,  
259 *Hmgcs1*, *Idi1*, *Opalin*, and *Trf*. Genes used for the reactive astrocyte score were *Serpina3n*, *C3*, *Emp1*,  
260 *Gfap*, *Ggta1*, *H2-T23*, *Cd109*, *Hspb1*, and *Icn2*. Genes used for the reactive microglia score were *Lpl*,  
261 *Cst7*, *Ptprc*, *Trem2*, *Lgals3*, *Axl*, *Lyz2*, *Clec7a*, *Spp1*, *Cst7*, and *Apoe*.

262 **Ligand-Receptor (LR) Analysis**

263 We performed ligand-receptor (LR) interaction analysis on the raw gene expression datasets  
264 using CellChat v2 (RRID:SCR\_021946) (Jin et al., 2023). For each experimental condition, spatial  
265 coordinates were aggregated, and an average spot size was computed to normalize the interaction  
266 distances. Coordinates from individual replicates were appropriately translated to prevent overlap and  
267 maintain the spatial integrity of the samples. The preprocessed data was then converted to a CellChat  
268 object, which encapsulated the gene expression matrix, cellular metadata, and spatial coordinates. In our

analysis, we grouped cells based on both Cell Type and Cell Subtype classes and incorporated spatial data to contextualize cell interactions within the tissue architecture. We then aligned our gene expression data with established molecular communication networks to predict potential LR and in turn cell-cell interactions. The likelihood and extent of intercellular signaling interactions was estimated by assessing the expression of LR pairs. Truncated mean calculation for average gene expression per cell group and bootstrapping for statistical inference were performed to ensure estimation robustness. The communication probabilities were calculated, accounting for the effect of spatial distance on signaling potential by adjusting for the scaled interaction range and considering contact-based nearest neighbor interactions. Subsequently, pathways were aggregated, and centrality analysis was performed to identify key nodes within the communication network. To explore the differential intercellular communication networks between HX and NX, data from both conditions were integrated. Differential expression analysis was then carried out to identify genes that displayed significant changes in expression levels, with a threshold of  $p\text{-value} < 0.01$ . Changes in ligand and receptor expression level, with a  $|\log_2(FC)| > 0.25$  were considered significant.

**Code Accessibility**

The custom code for cell proximity analysis has been uploaded to GitHub: [https://github.com/keon-arbabi/spatial\\_hypoxia/blob/main/keon\\_spatial\\_analyses.R](https://github.com/keon-arbabi/spatial_hypoxia/blob/main/keon_spatial_analyses.R)

**Tissue preparation and immunofluorescence staining**

Brains were harvested from P20 HX and NX exposed mice, fixed in 4% paraformaldehyde (PFA) for 24 hours at 4°C, washed 3 times with PBS, stored in 30% sucrose in PBS for at least 48 hours at 4°C, embedded in optimum cutting temperature (O.C.T.) mounting medium (Tissue-Tek), and stored at -80°C. Frozen embedded brains were sectioned coronally at 20um and stored at -80°C. For immunofluorescence staining, brain sections were first dried for 20 minutes at 37°C, washed 3 times with PBS, incubated in blocking solution containing (10% BSA, 6% normal donkey serum, 0.1% Triton X-100 for 1 hour at RT, then incubated in primary antibody solution containing 1:500 anti-NCAN (Cedarlane, Cat: AF5800-SP) diluted in blocking buffer overnight at 4°C. Sections were then washed 3 times with PBS-T (0.1% Triton X-100 in PBS) and incubated in Alexa Fluor 555 labelled secondary antibody solution

296 (1:500 diluted in PBS-T, ThermoFisher, Cat: A-21436) for 1 hour at RT. Sections were then washed 3  
297 times with 0.1% Triton X-100 and mounted with Fluoromount mounting medium with DAPI  
298 (ThermoFisher, Cat: #00-4959-52).

### 299 **Immunofluorescence Imaging**

300 Immunofluorescence stained slides were scanned on a 3DHistech Pannoramic 250 Flash III Slide  
301 Scanner using a Zeiss 40 × 0.95 NA objective. The instrument was operated in extended focus mode  
302 (seven focal planes spanning a 5-μm axial distance) to capture the entire cell volume across each tissue  
303 section. The microscope is housed in the Imaging Facility at The Hospital for Sick Children in Toronto  
304 (ON, Canada).

### 305 **NCAN fluorescence Intensity Analysis**

306 Immunofluorescence images were imported to the HALO Image Analysis Platform (Indica Labs,  
307 v.3.5.3577.173) for analysis. To quantify differences in NCAN distribution across the depth of the cortex,  
308 the cortex of each coronal section (from pia to corpus callosum) was manually segmented into three  
309 approximately equidistant regions encompassing the superficial cortical layers, middle cortical layers, and  
310 deep cortical layers. Average fluorescence intensity was quantified using the HALO Area Quantification  
311 FL module for each region.

312

## 313 **RESULTS**

314 We employed a widely used mouse model of chronic sublethal HX to investigate the brain's  
315 regenerative response to neonatal injury (Figure 1A, experimental schema). Mouse litters were exposed  
316 to 10% oxygen (HX) or 21% oxygen (normoxia, NX) between P3-11 (see *Methods*), a developmental  
317 period in mice that resembles the third gestational trimester in humans (Semple et al., 2013). Mouse  
318 dams were rotated daily between NX and HX conditions to avoid any confounding based on maternal  
319 care or nutrition. All mice were then moved to an environment with normal levels of oxygen until they  
320 were sacrificed at P21 (see *Methods*). We focused specifically on P21 as it represents a peak time during

the post-injury repair period (Fagel et al., 2006; Forbes et al., 2020; Jablonska et al., 2022; Salmaso et al., 2014).

We performed multiplexed error-robust fluorescence *in situ* hybridization (MERFISH) on coronal brain sections from three HX and three NX mice (see *Methods*). An RNA probe panel of 497 genes (Extended Data Table 1-1) was selected to enable the identification of major forebrain cell types as well as components of biologically relevant pathways including growth factors, Wingless-related integration site (WNT)/ $\beta$ -catenin, bone morphogenic protein (BMP), immune recognition and regulation, perineuronal net components, and senescence-associated genes (see *Methods*). Cells were segmented using an established deep-learning algorithm, CellPose 2.0 (Pachitariu and Stringer, 2022), to predict cell boundaries based on DAPI, a nuclear stain, and PolyT, an mRNA stain (see *Methods*). After segmentation, transcript counts were normalized by volume and quality control filtering was performed to remove segmented cells with abnormal physical size, low total number of transcripts, and potential doublets (Figure 1A, see *Methods*). The resulting dataset, encompassing all replicates and all regions, had a median volume of 179.5  $\mu\text{m}^3$  per cell and a median expression of 285.6 transcripts per cell.

Each coronal MERFISH image of the mouse brain was labeled based on region-specific marker genes and anatomic landmarks to define regions for downstream analysis (Figures 1B-C). After normalizing each sample, we independently integrated and analyzed cells from select regions including the cortex, corpus callosum, SVZ, caudate putamen (CP), lateral septal nucleus (LS), anterior commissure (Aco), and septal white matter tracts (SWM), respectively, across all datasets. Highly variable genes were used to compute principal components for uniform manifold approximation and projection (UMAP) and shared nearest neighbor clustering. After filtering, the final datasets included 668,947 cortex, 8,708 corpus callosum, 10,754 SVZ, 83,235 CP, 19,088 LS, 4,311 Aco, and 12,837 SWM cells across all samples, for a total of 807,880 transcriptionally profiled cells in these regions (Figures 2B-C, 3A, 3D, and Extended Data Figure 2-1A-D). Our analyses focused on the cortex, corpus callosum, and SVZ, given their relevance to HX injury and ample cell numbers, contributing statistical power to our findings. The number of unique genes and transcripts per cell for these three regions are displayed in Extended Data Figure 2-2A-F.

## 349 **Cell type identification by MERFISH**

350 A major benefit of high-resolution spatial transcriptomics is the potential to characterize cell type  
351 diversity within defined anatomical borders. As such, we analyzed each major anatomic region  
352 independently to ascertain region-specific cell type composition and spatially restricted cell types. In the  
353 cortex and corpus callosum, we classified cells at two levels of cell-type resolution. First, we identified  
354 broad cell type categories (referred to as “Cell Types”), then each Cell Type group was further sub-  
355 clustered to identify more specific subtypes or region-specific cell states (the “Cell Subtypes”). SVZ cells  
356 were classified at one level of resolution which included mostly broad cell type categorizations with the  
357 exception of NSC subtypes. Other regions such as the CP, LS, ACo and SWM, that were not analyzed in  
358 depth in this paper, were classified at one level of resolution with broad categories using the same criteria  
359 described below for Cell Types in the cortex and corpus callosum. Unless otherwise specified, genes  
360 used for characterizing cell types were selected from well-known and widely used brain cell-type  
361 markers.

362 For cortex and corpus callosum, Cell Types included non-neuronal cells corresponding to OL-  
363 lineage cells, vascular and perivascular cells (from here on collectively termed vascular cells), astrocytes,  
364 and microglia; and neuronal cells present only in the cortex, corresponding to excitatory neurons and  
365 interneurons. These included clusters of OL-lineage cells identified with markers such as *Olig1*, *Olig2*,  
366 *Sox8*, and *Sox10*; clusters of astrocytes identified with *Aqp4* and *S100b*; clusters of vascular cells  
367 identified with at least one of *Pecam1*, *Col1a1*, or *Pdgfrb*; and microglia identified with *Cx3cr1* (Figure 2A-  
368 B for cortex and 3A-B for corpus callosum). In the cortex only, clusters of excitatory neurons were  
369 identified with high expression of *Slc17a7* along with some other excitatory neuron genes like *Neurod2*  
370 and the layer-specific markers described later while interneurons were identified with *Gad1* and *Gad2*  
371 (Figure 2C-D).

372 Next, each Cell Type group in the cortex and corpus callosum was subsetted and independently  
373 clustered to identify distinct clusters for subclassification into Cell Subtypes. In the cortex, interneurons  
374 formed three subtype clusters (Extended Data Figure 2-3A), each enriched for known markers of



interneuron subpopulations: *Pvalb* (Int 1), *Sst* (Int 2), and *Prox1* (Int 3) (Figure 2D). Int1 and Int2 were spatially concentrated in middle to deeper cortical layers whereas Int3 was concentrated in upper cortical layers (Figure 2I). Excitatory neurons formed 10 clusters (Extended Data Figure 2-3B) which were annotated based on their spatial distribution in the cortex (Figure 2J) and expression of known cortical layer markers (Figure 2D). These included a cluster of cells that were spatially concentrated in cortical layers I-III and expressed *Cux2* and *Mef2c* (Exc-1,2,3); a cluster of cells spatially concentrated in cortical layers II and III which expressed high *Cux2*, *Mef2c*, *Satb2*, and *Lmo4* (Exc-2,3); a cluster of cells spatially concentrated in cortical layers II-IV and expressed *Mef2c* and *Lmo4* (Exc-2,3,4); a cluster of cells spatially concentrated in cortical layers II-IV and all three layers of the piriform cortex and expressed low levels of *Mef2c* and *Lmo4* (Exc-2,3,4,P); a cluster of cells spatially concentrated in piriform layer 1 and expressing *Mef2c*, *Lmo4*, *Bcl11b*, *Foxo1*, and *Cntn6* (Piri1); a cluster of cells spatially concentrated in cortical layers V and expressing *Dkk3*, *Foxp1*, *Lmo4*, *Satb2*, and *Mef2c* (Exc5); a cluster of cells spatially concentrated in cortical layers V and VI and expressing *Tle4*, *Dkk3*, and *Fezf2* (Exc-5,6); a cluster of cells spatially concentrated in cortical layer VIb and piriform layers 2 and 3, and expressing *Nr4a2* (Exc-6b,P2,3); a cluster of cells spatially concentrated in cortical layers 6b and the subplate, and expressing *Ccn2*, *Tle4*, *Nr4a2*, *Satb2*, and *Rgs8* (Exc-6b,SP); and a cluster of cells spatially concentrated in the subplate and expressing *Nr4a2*, *Dkk3*, *Lmo4*, *Satb2*, *Mef2c*, and *Cux2* (SP) (Extended Data Figure 2-3B and Figures 2D, and 2J).

OL-lineage cell clusters in the cortex (Figure 2A) and corpus callosum (Figure 3B) were classified as OPCs if they expressed *Pdgfra*, and OLs if they expressed *Mag* and no *Pdgfra*. OPCs formed one distinct cluster in the corpus callosum (Extended Data Figure 3-1A), but two clusters in the cortex (Extended Data Figure 2-3C). In both regions, OLs formed multiple clusters corresponding to different stages of lineage progression with graded expression patterns of the canonical OL marker *Mag* and other genes described in previous studies as necessary for and upregulated at different stages of OL development. OL clusters with the lowest expression of *Mag* and moderate to high enrichment of OL differentiation and early marker genes *Fyn* (Osterhout et al., 1999) and *Gpr17* (Fumagalli et al., 2011) were classified as newly formed OLs (OL-new); clusters with high enrichment for *Fyn*, *Gpr17*, and other

OL differentiation genes such as *Tcf7l2* (Guo and Wang, 2023) and *Myrf* (Bujalka et al., 2013) were classified as immature OLs (OL-immat); and clusters with the highest expression of *Mag* and enriched for mature, myelinating OL genes *Trf* (Bujalka et al., 2013), *Car2* (Floriddia et al., 2020), and *Opalin* (Marques et al., 2016) were classified as mature OLs (Figure 2A and Extended Data Figure 2-3C for cortex and Figure 3B and Extended Data Figure 3-1A for corpus callosum). OLs in the cortex, particularly OL-immat and OL-mat, were enriched in the deeper layers (Figure 2E). In the corpus callosum, OL-new was enriched ventrally (Figure 3C', 3C''), in regions adjacent to the SVZ. This suggests that these newly formed OLs appear to migrate from the SVZ towards the corpus callosum.

Astrocyte clusters were subclassified as reactive astrocytes if they expressed high *Gfap* and were differentially enriched for at least two of the reactive astrocyte markers *Serpina3n*, *Ggta1* (Liddelow et al., 2017), and *C3* (Clarke et al., 2018), and classified as homeostatic astrocytes otherwise in both the cortex (Figure 2A and, for better visualization, Extended Data Figure 2-3E) and corpus callosum (Figure 3B and Extended Data Figure 3-1C). In the cortex, reactive astrocytes formed two clusters (Extended Data Figure 2-3D), with one population (Astro-react1) distributed throughout the cortex and meninges, and the second population (Astro-react2) concentrated in the meninges (Figure 2F). Analysis of differentially expressed genes (DEGs) between these two clusters revealed that Astro-react1 was enriched for *Gria2*, *Vcam1*, *Sox9*, and *Notch1/2*, and Astro-react2 was enriched for *Gfap*, *S100b*, and *Sparc* (Figure 2A). In the corpus callosum, we identified one cluster of reactive astrocytes (Astro-react) which, like Astro-react1 of the cortex, differed from the meninge-enriched astrocytes with their high expression of *Vcam1* and *Sox9* (Figure 3B and Extended Data Figure 3-1B). In both the cortex (Figure 2A and Extended Data Figure 2-3D) and corpus callosum (Figure 3B and Extended Data Figure 3-1B) we identified three clusters of homeostatic astrocytes (Astro-hom1, Astro-hom2, Astro-hom3). Similar naming of these clusters in the two regions does not imply transcriptomic similarity.

Microglia clusters in the cortex (Figure 2A) and corpus callosum (Figure 3B) were subclassified as reactive microglia if they expressed high levels of the reactive microglia marker *Trem2* or subclassified as homeostatic microglia otherwise. Cortical microglia formed one homeostatic cluster (Micro-hom) and two reactive clusters (Extended Data Figure 2-3F) whereas corpus callosum microglia formed one

homeostatic (Micro-hom) and one reactive cluster (Micro-react) (Extended Data Figure 3-1D). Microglia subtypes were distributed throughout the cortical layers (Figure 2G) and corpus callosum (Figure 3C', 3C'').

Vascular cell clusters in the cortex (Figure 2A) and corpus callosum (Figure 3B) were subclassified as pericytes (Peri) if they expressed high levels of pericyte markers *Pdgfrb* and *Atp13a5*, fibroblasts (Fibro) if they expressed high levels of fibroblast markers *Col1a1* and *Col1a2*, and endothelial cells if they expressed high levels of endothelial cell markers *Pecam1*, *Esam*, and *Cdh5*; low levels of pericyte and fibroblast markers. Pericytes formed only one cluster in both cortex (Extended Data Figure 2-3G) and corpus callosum (Extended Data Figure 3-1E). In the cortex, fibroblasts formed four clusters (Extended Data Figure 2-3G). In general, there was a higher density of fibroblasts in the meninges compared to the cortex, but one cluster in particular. Fibro-1 was highly concentrated in the meninges (Figure 2H). Compared to the other fibroblast clusters, Fibro-1 was differentially enriched for genes like *Cxcl12*, *Gfap*, and *Pdgfra* (Figure 2A). In the corpus callosum, fibroblasts formed one distinct cluster (Extended Data Figure 3-1E). Endothelial cells formed three clusters in the cortex (Extended Data Figure 2-3G) and formed two clusters in the corpus callosum (Extended Data Figure 3-1E).

In the SVZ, we identified vascular cells, microglia, ependymal cells, slowly-proliferating neural stem cells (NSCs), transit amplifying progenitors (TAPs), OPCs, and neuroblasts (Figure 3D). Slowly-proliferating NSCs were identified by their expression of known and recently established SVZ NSC markers *Vcam1*, *Thbs4*, *Tspan18*, and *Slc1a3* (Borrett et al., 2020) and absence of *Mki67*, TAPs by their expression of *Mki67*, *Egfr*, *Ascl1* and *Dlx2*, neuroblasts by their expression of *Dlx2* and *Dcx* and absence of *Ascl1*, and ependymal cells were identified by their expression of *Foxj1* (Figure 3E). Iterative clustering of NSCs revealed 3 clusters (Extended Data Figure 3-1F): one cluster was enriched for *Crym*, a ventral SVZ (ganglionic eminence) marker (Borrett et al., 2020), and spatially enriched along the ventrolateral wall of the SVZ (NSC-vent); one cluster was enriched for the known NSC gene *Tnc* and spatially enriched along the dorsal wall of the ventricle (NSC-dors); and the third cluster was enriched for *Ednrb*, a recently characterized SVZ NSC gene (Yuzwa et al., 2017), and spatially enriched along the septal wall of the ventricle (NSC-sept) (Figure 3E and 3I). Of the two neuroblast clusters, one was classified as

456 olfactory bulb neuroblasts (NB-OB) for its expression of *Sp8*, a marker that is prominent in most  
457 neuroblasts destined for the olfactory bulb (Gaborieau et al., 2018) (Figure 3E). The other neuroblast  
458 cluster (NB) may represent those that will migrate either to the olfactory bulb or to the caudoputamen  
459 (Bordiuk et al., 2014; De Marchis et al., 2004).

460

461 **Region-specific patterns of signaling-related gene expression in the NX brain**

462 Recent studies have suggested that cellular phenotypes are at least partly informed by spatial  
463 location in the brain (Allen et al., 2023; Stogsdill et al., 2022; Zhang et al., 2021). Before investigating  
464 how HX alters region-specific cellular signaling profiles, we first compared transcriptional profiles of non-  
465 neuronal cells between distinct brain regions (SVZ, corpus callosum, superficial layers of the cortex, and  
466 deep layers of the cortex) in the P21 NX brain to identify baseline regional heterogeneity. This was done  
467 by differential gene expression analysis where a false discovery rate (FDR) < 0.05 and log<sub>2</sub> fold-change  
468 (log<sub>2</sub>(FC)) > 0.25 were used to identify statistically significant differences in each comparison (see  
469 *Methods*). We observed extensive differences in signaling-related gene expression levels across all  
470 regions and cell types.

471 Notably, vascular cells were remarkably different between the upper and deep cortical layers with  
472 respect to expression of genes involved in WNT, Insulin-like growth factor (IGF), BMP, and fibroblast  
473 growth factor (FGF) signaling. Upper cortex vascular cells were enriched for expression of *Fzd1/2/7*,  
474 *Wnt4/5a*, *Sfrp1*, *Igf2*, *Igfbp2*, *Bmp4/5/7*, *Fgf1*, *Fgfr1*, and *Fgfr2*, while deep cortex vascular cells were  
475 enriched for expression of *Igf1r* and *Apc* (Extended Data Figure 4F and Extended Data Table 5-1).  
476 Compared to the corpus callosum and SVZ, vascular cells of the upper cortex but not the deep cortex  
477 were enriched for WNT ligand (*Wnt5a*), BMP ligand (*Bmp4/5/7*), and IGF ligand (*Igf2*, *Igfbp2*) genes  
478 (Extended Data Figure 4B-F and Extended Data Table 5-1). These results suggest activation of the  
479 canonical WNT pathway within vascular cells in the upper cortex, and robust WNT inhibition mediated by  
480 the negative regulator *Apc* within vascular cells in the deep cortex of the NX brain.

481 OPCs in different regions exhibited unique patterns of signaling-related gene expression. For  
482 example, SVZ and corpus callosum OPCs expressed higher levels of *Bmp4* and *Notch1*, while cortical

OPCs expressed higher levels of *Cx3c1* (Extended Data Table 5-1). Microglia also showed notable differences between regions in the NX brain. SVZ microglia exhibited higher expression of genes involved in WNT signaling, such as *Fzd1/2/5/8*, *Lrp4/6/8*, *Sfrp1*; genes involved in sonic hedgehog (SHH) signaling such as *Ptch1*, *Gli1/3*; and Ephrin signaling genes such as *Efna2*, *Efnb2/3*, *Epha4*, and *Ephb1* compared to the corpus callosum, deep cortex, and upper cortex (Extended Data Figure 4A-C and Extended Data Table 5-1). This may suggest that in the postnatal mouse brain, microglia in the SVZ are uniquely suited for sensing and regulating the SVZ niche to modulate neurogenesis (Ribeiro Xavier et al., 2015)

### **HX-associated changes in cellular composition**

We next assessed differences in global cell type proportions between HX and NX by leveraging the multiple biological replicates for each condition (see *Methods*). In the corpus callosum, we found that the proportion of newly formed OLs was markedly reduced following HX (42% reduction,  $p = 0.016$ ), while the proportion of OPCs was significantly increased (72% increase,  $p = 0.025$ ; Figure 3F-G). These findings corroborate the idea that chronic sublethal neonatal HX induces WMI followed by a robust period of oligodendrogenesis (Fagel et al., 2006; Jablonska et al., 2022). However, we did not detect a significant change in the proportion of any OL-lineage Cell Subtypes in the cortex (Figure 2L). This could imply that OL lineage cells in the cortex are less severely affected by HX.

We also observed a significant increase in the proportion of reactive astrocytes in the corpus callosum in HX (32% increase,  $p = 0.037$ , Figure 3F). This is consistent with previous work showing that there is an increase in the number of C3-expressing reactive astrocytes in the corpus callosum following acute perinatal WMI (Back and Rosenberg, 2014; Renz et al., 2022). In the cortex, we did not observe a significant change in the proportion of reactive astrocytes, but the proportion of Astro-hom3 was significantly reduced (21% reduction,  $p = 0.044$ ).

In the cortex of HX mice, we identified a significant increase in the abundance of Endo-1 cells, the most abundant subpopulation of endothelial cells (45% increase,  $p = 0.015$ , Figure 2M), suggestive of vascular remodeling.

Lastly, we observed a significant increase in the proportion of a large population of excitatory neurons in layer II-III (14% increase,  $p = 0.019$ ), and a significant decrease in a small population of excitatory neurons in layers I-III (51% reduction,  $p = 0.049$ , Figure 2K), indicating a change in the cell type composition of upper layer excitatory neurons. We also observed an increase in the proportion of Int1, a population of cortical interneurons (12% increase,  $p = 0.038$ , Figure 2K). An increase in cortical neurons could suggest a disruption or delay in programmed neuron death and clearing in the middle-upper cortical layers (the last layers to form and mature), a process that largely takes place in the first week after birth, coinciding with the timing of HX exposure (Castillo-Ruiz et al., 2020; Pfisterer and Khodosevich, 2017). No significant change was observed in the proportion of SVZ cell types (Figure 3H).

### **Proximity analysis reveals widespread HX-associated changes in local cellular architecture**

We next evaluated changes in local cellular neighborhood composition associated with neonatal HX. Unlike spot-based spatial transcriptomics methods, MERFISH enables us to accurately map both spatial locations and transcriptional identities of individual brain cells. We leveraged this information using a novel computational approach for quantifying condition-associated differences in local cell type proximities (see *Methods*), which addresses some limitations of existing methods (Dries et al., 2021; Palla et al., 2022). Briefly, we calculated the condition-related differences in the proportion of cells of one type in the vicinity of a second type, thus capturing asymmetrical differences in local proportions between cell types. For example, our approach can detect the depletion of astrocytes surrounding neurons when the reverse is not true. Second, we directly compare cell type proximities between conditions using a general linear mixed effects model, accounting for the statistical non-independence of measures from the same tissue sample when there are multiple biological replicates (see *Methods*). We applied this approach at the microscale, capturing local changes in proximity that matter for cellular interaction, however, we note that such differences may also reflect global cellular abundance differences between conditions (e.g., those shown in Figure 2K-M and 3F-H).

In the cortex, neonatal HX was associated with decreased proximity of homeostatic astrocytes to several cell types (Figure 4A), including OPC2 ( $\beta = -0.46$ ,  $\text{FDR} = 8.45 \times 10^{-5}$ ; Figure 4D), newly formed

OLs ( $\beta = -0.48$ ; FDR = 0.012), and immature OLs ( $\beta = -0.43$ , FDR =  $4.21 \times 10^{-3}$ ). This may indicate a disruption in the supportive interactions provided by astrocytes, such as the secretion of local factors (e.g. BDNF, CNTF) that promote OL maturation and myelination during healthy conditions and following injury.(Miyamoto et al., 2015) HX induced dramatic changes in the proximity of different populations of cortical excitatory neurons to other neurons and non-neuronal cells. For example, after HX, a population of upper layer excitatory neurons, Exc-1,2,3, had decreased proximity to interneurons (Int-3,  $\beta = -0.15$ , FDR =  $6.65 \times 10^{-6}$ ), reactive ( $\beta = -0.06$ , FDR = 0.046) and homeostatic astrocytes ( $\beta = -0.13$ , FDR =  $1.07 \times 10^{-3}$ ), and OPC2 ( $\beta = -0.05$ , FDR =  $1.93 \times 10^{-3}$ ; Figure 4A).

In the corpus callosum following HX (Figure 4B), we observed significantly reduced proximity of newly formed OLs in the neighborhoods of several cell types, including OPCs ( $\beta = -0.37$ , FDR =  $6.82 \times 10^{-3}$ ; Figure 4E) and endothelial cells ( $\beta = -0.65$ , FDR = 0.011). Additionally, we observed reduced proximity of surrounding reactive astrocytes ( $\beta = -0.57$ , FDR =  $2.62 \times 10^{-13}$ ) and microglia ( $\beta = -0.45$ , FDR = 0.016) near homeostatic astrocytes. Such local interactions are likely essential for OL maturation and efficient myelination.(Miyamoto et al., 2015) The altered spatial organization of these cells potentially contributes to the impaired myelination characteristic of diffuse WMI.

In the post-HX SVZ, NSCs showed significantly increased proximity to differentiating neuroblasts ( $\beta = 0.28$ , FDR =  $7.12 \times 10^{-3}$ ), with a trending increase in proximity to OPCs, microglia, and vasculature (Figure 4C and 4F). These changes align with the roles of activated microglia in promoting oligodendrogenesis and neurogenesis. The closer association with vascular components may indicate an adaptive response to HX, possibly involving angiogenesis or enhanced metabolic support. Neuroblasts saw increased proximity to NSCs ( $\beta = 0.36$ , FDR =  $1.61 \times 10^{-4}$ ), microglia ( $\beta = 0.81$ , FDR =  $6.90 \times 10^{-4}$ ), and OPCs ( $\beta = 0.54$ , FDR = 0.026). These changes could reflect neural repair through enhanced interactions of neuroblasts with NSCs for proliferation, with microglia for inflammation resolution, and with OPCs for myelination, altogether accelerating recovery processes. Overall, these observations suggest a reorganization or adaptation of the SVZ niche in response to neonatal HX, highlighting the region's plasticity under developmental stress.

In total, our proximity analysis emphasizes a crucial spatial component to the effects of neonatal HX beyond gene expression. Changes were extensive and heterogeneous across cell types and regions, ranging from disrupted myelination in the corpus callosum to adaptive cellular reorganization in the SVZ.

### **Neonatal HX alters regional patterns of signaling-related gene expression**

We next analyzed cell type- and region-specific transcriptional changes between HX and NX conditions using differential gene expression analysis (see *Methods*). This comparative analysis aimed to identify molecular processes perturbed during HX exposure in the context of early brain development. In all cell type populations assayed in the SVZ, corpus callosum, and cortex, we found that the vast majority of significant DEGs were upregulated following HX (Figure 5A-C and Extended Data Table 5-1). While many genes exhibited widespread cell-type specific changes, many cells also shared DGEs within the forebrain regions (Figure 5D-F).

We expanded our findings from the differential gene expression analysis by focusing on understanding cell-cell signaling after neonatal HX. Neighboring cells communicate via secreted molecules (ligands) that can act on receptors in nearby cells. These ligand-receptor (LR) networks are fundamental signaling nodes that regulate circuit function and injury response. To understand how local cell-cell communication networks change in the context of neonatal brain injury, we performed a spatially-informed LR analysis using CellChat v2 (see *Methods*). We grouped predicted LR pairs based on whether signaling occurred within the same cell type (e.g., OPC to OPC; intra-lineage) or between different cell types (e.g., microglia to OPC; inter-lineage). After exposure to neonatal HX, we identified region-specific cellular programs governing regenerative oligodendrogenesis and neurogenesis.

In the SVZ, we found that HX induced an upregulation of *Egfr*, *Lmnb1*, and the proliferation marker *Mki67* within most SVZ cell types, including the neural progenitors NSCs, OPCs, and TAPs, suggestive of NSC activation (Figure 5G and Extended Data Table 5-1) (Koufi et al., 2023). In response to HX, neural progenitors also upregulated genes involved in OL differentiation such as *Qk* and *Ptprz1*, and neurogenic genes including *Dcx*, *Gria2*, and *Stmn1*, suggestive of increased neurogenic and gliogenic priming (Extended Data Table 5-1). We observed dramatic changes in BMP, WNT, and Notch



590 signaling in the SVZ, consistent with their role in regulating stem and progenitor cell maintenance,  
591 proliferation, differentiation, and fate decisions (Figures 5G and 6A-B, Extended Data Tables 5-1 and 6-  
592 1). Specifically, there was a significant increase in *Bmp7* expression in OPCs (Figures 5G) and an  
593 increase in BMP7 and BMP4 signaling from OPCs to OPCs, NSCs, TAPs, microglia, and vascular cells  
594 (Figure 6A-B). In addition, the WNT ligand *Wnt7a*, the receptor *Lrp6*, the effector *Ctnnb1*, and target gene  
595 *Ccnd1* all demonstrated increased expression in most SVZ cells, including NSCs, after HX (Figure 5G  
596 and Extended Data Table 5-1) which translated to a widespread increase in WNT signaling (Figure 6B  
597 and Extended Data Table 6-1). In the HX SVZ, *Notch1* and *Notch2* receptors were upregulated in most  
598 cell types, while the ligand genes *Dll1* or *Dll4* were upregulated in vascular cells, TAPs, and immune cells  
599 (Figure 5G and Extended Data Table 5-1) which translated to an increase in Notch signaling between  
600 these cell types (Extended Data Table 6-1). Interestingly, we found increased transforming growth factor  
601  $\beta$ -2 and 3 (TGF $\beta$ -2/3) signaling between the vasculature and microglia in the SVZ after HX (Figure 6B  
602 and Extended Data Table 6-1). TGF $\beta$  is a critical component of the microglial pro-neurogenic response  
603 (Battista et al., 2006; De Lucia et al., 2016; Makwana et al., 2007).

604 In the corpus callosum, we identified several signaling nodes that promote white matter recovery  
605 after neonatal HX, including upregulation of MAG to MAG and TGF- $\alpha$  to epidermal growth factor receptor  
606 (EGFR) signaling between Cell Subtypes of OL-lineage cells (Extended Data Table 6-1). We observed  
607 increased WNT signaling from astrocytes and OLs, increased IGF2/IGF1R signaling from vascular cells  
608 to astrocytes and OLs, and increased CNTN1-Notch signaling between OLs, astrocytes, and vascular  
609 cells (Extended Data Table 6-1). Changes in Notch signaling was a commonly identified theme in the  
610 corpus callosum: *Notch1* and *Notch2* were upregulated in astrocytes and OL-lineage cells and the ligand  
611 *Dll1* was upregulated in OL lineage cells (Figure 5G and Extended Data Table 5-1). Moreover, we found  
612 increased GAS6 signaling through its receptors (TAM receptors, encoded by *Tyro3*, *Axl*, *Mer*) between  
613 microglia and astrocytes, vascular cells, and OL-lineage cells (Extended Data Table 6-1). Following  
614 demyelinating injury, GAS6-TAM signaling promotes remyelination and glial cell development, including  
615 suppression of a deleterious (anti-regenerative) microglia response (Binder et al., 2011, 2008). Notably,  
616 we found evidence of neurovascular adaptation after HX, including upregulation of genes involved in cell

617 migration and vascular permeability (*Fstl1* and *Itgb1*) (Fujioka et al., 2017) in vascular cells in the corpus  
618 callosum, which may promote immune cell infiltration and/or guide the migration of new neurons and glial  
619 cells (Figure 5G and Extended Data Table 5-1). We observed an increase in inflammatory and migratory  
620 signaling from corpus callosum fibroblasts, including upregulation of Interleukin 34 (IL-34) to colony  
621 stimulating factor 1 receptor (CSF1R) and ephrin A1 (EFNA1) to Ephrin type-A receptor 7 (EphA7)  
622 ligand-receptor pairs, both of which may support glial scar formation (Figure 6C-D and Extended Data  
623 Table 6-1) (Bellver-Landete et al., 2019; Gerber et al., 2018; Zhou et al., 2023).

624 In the cortex, LR analysis was notable for a broad, multicellular increase in several signaling  
625 pathways previously implicated in brain circuit wiring and the response to injury. Endothelin-1  
626 (EDN1)/Endothelin Receptor Type B (EDNRB) signaling was increased between endothelial cells,  
627 fibroblasts, astrocytes, OLs, and microglia, and astrocytes (Extended Data Table 6-1). Endothelin  
628 regulates myelination capacity in OLs, as endothelin is upregulated after demyelination and directly  
629 inhibits OPC differentiation via astrocytes (Hammond et al., 2015). Additionally, we found that fractalkine  
630 (encoded by *Cx3cl1*)-CX3CR1 signaling, a regulator of gliogenesis, was increased between several non-  
631 neuronal cell populations, including OLs, OPCs, fibroblasts, and astrocytes, to reactive microglia  
632 (Extended Data Table 6-1). A regulator of fractalkine expression and remyelination, TGF $\beta$ 1 signaling,  
633 was also enhanced following HX between endothelial cells, fibroblasts, and microglia. Canonical WNT  
634 signaling is important for TGF $\beta$ -mediated fibrosis (Akhmetshina et al., 2012), and we identified increased  
635 WNT signaling in deep layer cortical excitatory neurons (WNT4 with FZD4), as well as between vascular  
636 cells, deep layer excitatory neurons and astrocytes (WNT7A with FZD4). We observed a HX-induced  
637 increase in cytokine signaling (including IGF2-IGF1R, IGF2-IG2R, fractalkine-CX3CR1, TGFB1-TGFBR1,  
638 TGFB3-TGFBR1 ligand-receptor pairs) largely sourced by fibroblasts and other vascular cells, and  
639 targeting vascular cells and microglia (Figure 6E-F and Extended Data Table 6-1). Thus, vascular cells  
640 may represent an important source of inflammatory signaling leading to increased microglial activation  
641 after neonatal HX. Additionally, several homophilic (CDH5-CDH5, ESAM-ESAM, PECAM1-PECAM1)  
642 and heterophilic (FGF1/2-FGFR1/2R, BMP4/7-BMPR1A, VEGFA-FLT1) endothelial interactions involved  
643 in regulating vascular development and blood brain barrier permeability integrity were dysregulated in all

three regions of the brain (Figure 6A-F and Extended Data Table 6-1) (Argaw et al., 2012; Klimaschewski and Claus, 2021; Knox et al., 2022; Li et al., 2018). In addition, in the cortex, we found that HX induced an upregulation of *Sst* expression in interneurons and an upregulation of *Sstr2* expression in both interneurons and excitatory neurons (deep and superficial layers). Furthermore, LR analysis revealed increased SST-SSTR2 signaling from interneurons to other neurons following HX (Extended Data Table 6-1), all of which could impact excitatory-inhibitory neuron balance.

Ephrin communication was commonly altered across the cortex, SVZ, and corpus callosum. Cortical excitatory neurons and interneurons in the HX brain showed an upregulation of receptors *Epha4*, *Epha6*, and *Epha7* and ligands *Efnb2* and *Efnb3* (Figure 5G and Extended Data Table 5-1). EFNA1 signaling by cortical fibroblasts to OL-lineage cells and astrocytes was significantly upregulated post-HX (Extended Data Table 6-1). In the SVZ, there was widespread upregulation of ephrin genes; for example, *Epha4* and *Efnb2* were upregulated in all cell types following HX (Extended Data Table 5-1). Furthermore, all SVZ cells participated in ephrin signaling as sources and targets following HX. The OL-lineage in the corpus callosum also upregulated ephrin genes and showed increased ephrin signaling targeting all major Cell Types (Extended Data Table 6-1). EFNA1 interacts with EphA4 to inhibit OL process extension via ephexin1-RhoA-Rock-myosin 2 (Harboe et al., 2018). These HX-induced ephrin interactions may play an important role in guiding the migration and process extension of injury-responsive glial cells or new neurons.

Another important source of cell guidance signaling is the extracellular matrix. In particular, chondroitin sulfate proteoglycans (CSPGs) are extracellular matrix components known regulate cell migration, synapse formation and maturation, and inflammation in the developing brain (Dyck and Karimi-Abdolrezaee, 2015; Siebert et al., 2014). However, the upregulation of CSPGs following brain injury has been shown to block migration of neuroblasts and inhibit regeneration (Luo et al., 2022; Siebert et al., 2014). We found that OL-lineage cells and astrocytes in the cortex and corpus callosum, cortical excitatory neurons, cortical interneurons, and all SVZ cell types showed an upregulation of some CSPG genes such as *Vcan*, *Ncan*, *Bcan*, and *Tnr* (Figure 5G and Extended Data Table 5-1). To examine whether the increase in CSPG gene expression correlated with an increase in protein levels, we

671 performed immunofluorescence staining for NCAN in the P21 brain. We found that the average positive  
672 fluorescence intensity of NCAN staining over area was significantly higher across the HX cortex  
673 compared to NX (Figure 5H-I). Furthermore, the significant increase in NCAN fluorescence intensity was  
674 true across the superficial, middle, and deep cortical layers (Figure 5J). These results indicate an  
675 increase in neural guidance cues in the extracellular matrix that could affect the appropriate migration  
676 and integration of new cells in the HX brain.

677

### 678 **Neonatal HX is associated with changes in region-specific cell states**

679 Finally, we asked whether microglia, astrocyte, and OL-lineage cell state is dictated by spatial  
680 context by comparing gene expression patterns between the SVZ, corpus callosum, and cortex.  
681 Differential gene expression analysis revealed notable differences in cell state associated gene  
682 expression across different anatomical regions in the NX brain. OL-lineage cells in different regions  
683 showed different levels of gene expression for OL differentiation and maturation related genes. OPCs in  
684 the SVZ (Figure 7A-B) and corpus callosum (Figure 7D-E) had higher levels of many oligodendrogenesis  
685 genes including *Olig2*, *Gpr17*, *Itpr2*, and *Fyn* compared to both superficial and deep layer cortical OPCs.  
686 Following HX, these genes were upregulated in SVZ OPCs while only some (i.e., *Gpr17*) were  
687 upregulated in corpus callosum OPCs (Figure 5K and Extended Data Table 5-1). To characterize the  
688 overall differentiation and maturation state of OL-lineage cells, we used several established genes  
689 (Floriddia et al., 2020; Marques et al., 2016; Takeuchi et al., 2020) to calculate scores for OL  
690 differentiation priming ("OL genesis"), and OL maturation. We found that OPCs in the SVZ and corpus  
691 callosum had a higher OL genesis score than cortical OPCs (Figure 7F). Similarly, newly formed OLs in  
692 the corpus callosum had a higher OL genesis score than in the cortex (Figure 7G). Following HX, there  
693 was a trending but statistically not significant increase in the OL genesis scores among OPCs in the SVZ  
694 and corpus callosum, as well as in newly formed OLs in the corpus callosum (Figure 7F-G). The OL  
695 maturation score was higher in the corpus callosum than the superficial and deep cortical layers for OL  
696 lineage cells altogether (Figure 7H) and specifically in immature (Figure 7I) and mature OLs (Figure 7J).  
697 This score also showed a trending but not significant increase in upper cortical OLs following HX (Figure

7H-J). Overall, these results suggest regional differences in the maturation dynamics between corpus callosum and cortical OLs. However, the weak effect of HX on oligodendrogenic potential and maturation suggests that myelination impairments associated with DWMI may have less to do with OL dysfunction and more with the influence of their cellular environment.

In the both NX and HX brains, all astrocytes in the corpus callosum had significantly higher expression of *Gfap* than astrocytes in the cortex, with Astro-react also exhibiting higher levels of reactive markers *Ggta1* and *Serpina3n* in the corpus callosum (Figure 7K-M). Following HX, all astrocytes in the cortex, but not corpus callosum upregulated *Gfap* (Figure 5L). We then calculated astrocyte reactivity scores from established reactive astrocyte genes (Liddel et al., 2017; Matusova et al., 2023; Zamanian et al., 2012) and found that astrocytes in the NX corpus callosum exhibited a significantly higher state of reactivity compared to those in the cortex. This heightened reactivity was not altered by HX treatment. Within the cortex, astrocytes in the superficial layers showed a slightly elevated reactivity score over those in the deep layers (Figure 7N-P). Astro-hom, on the other hand, had higher *Sparc* expression in the cortex than in the corpus callosum, with deep layer astrocytes expressing more *Sparc* than superficial ones, a trend maintained post-HX (Figure 7K-M). Since *Sparc* encodes a secreted protein that negatively regulates synaptogenesis (Kucukdereli et al., 2011), this emphasizes the specialized function of cortical astrocytes in synapse formation and neural homeostasis.

Differential gene expression analysis revealed that microglia in both the NX and HX SVZ and corpus callosum exhibited a significantly lower expression of both *Tmem119* and *Trem2* compared to microglia in the superficial cortex and deep cortex (Figure 7Q-T). SVZ microglia showed the same trend of lower expression of both *Tmem119* and *Trem2* when compared to the corpus callosum (Figure 7Q). This trend is unexpected because it is widely acknowledged that *Tmem119* has higher expression in homeostatic microglia while *Trem2* is higher in reactive microglia (Boche and Gordon, 2022). However, recent work showing that *Tmem119* gene expression levels and spatial distribution in the brain are incongruent with protein levels following traumatic brain injury challenge the use of transcriptomic *Tmem119* as a marker for homeostatic microglia (Mercurio et al., 2022). Therefore, to better characterize the reactivity state of microglia across different regions, we calculated reactivity scores using multiple

genes shown previously to be specific to or enriched in reactive microglia at the transcriptomic level (see *Methods*) (Paolicelli et al., 2022; Wahane et al., 2021). We observed a lower reactivity score in corpus callosum microglia, specifically Micro-react, compared to superficial cortex microglia (Figure 7U-W). HX exposure reduced the reactivity score of corpus callosum microglia significantly, pushing microglia reactivity in the corpus callosum to be significantly lower than both upper and deep cortex microglia. In addition, only microglia in the SVZ exhibited a significant change in state related genes following HX exposure, including an upregulation of homeostatic microglia-associated *Tmem119* and reactive marker *Lgals3* (Figure 5M).

733

## 734 **DISCUSSION**

Advances in the care of very low birthweight preterm infants have markedly improved survival. However, despite these advances, survivors of preterm birth continue to have high propensity for developmental delay and disability. Chronic HX exposure resulting from an underdeveloped respiratory system leads to cerebral WMI, a major cause of neurodevelopmental disorders in preterm infants, including cerebral palsy. However, the underlying cellular mechanisms that govern the brain's response to HX and recovery from WMI remain poorly understood. Here, we employed high-resolution spatial transcriptomics as a discovery platform to map cell type- and region-specific transcriptional signatures during recovery from neonatal HX. At baseline (NX condition), we identified several brain region-specific cell states, including spatially restricted populations of glia and vascular cells that play a key role in modulating the signaling environment and may regulate developmental processes such as neurogenesis and gliogenesis, cell migration, synapse formation, and inflammation. We found that during the reparative phase following neonatal HX exposure, there were changes in regional cell type composition, neurogenic and gliogenic transcriptional programs, and local cellular architecture, which are likely the result of extensive changes in regional signaling networks. Thus, our results support a model of niche cell states and signaling networks that are region- and stimulus-dependent.

First, we demonstrate that at baseline, OPCs in the neurogenic niche and white matter have a transcriptomic profile that is more proliferative and more primed for differentiation than in the cortex. In

752 response to HX, OPCs within the neurogenic niche further upregulate proliferation-associated genes and  
753 genes encoding ligands that modulate OL formation and myelination. We found that OPCs upregulated  
754 BMP ligand genes such as *Bmp4* which, in the context of demyelinating injury, has been shown to be  
755 produced by injury-activated OPCs and inhibit the differentiation of OPCs to OLs (Ulanska-Poutanen et  
756 al., 2018). We also observed upregulation of *Cx3c1*, which encodes fractalkine, from several glial cell  
757 types including OL-lineage cells to reactive microglia. Fractalkine has an established pro-regenerative  
758 role in remyelination, particularly via OPCs and microglia (de Almeida et al., 2023; Ridderstad Wollberg  
759 et al., 2014). Interestingly, previous work has shown that environmental enrichment both enhances  
760 recovery from neonatal diffuse WMI and increases fractalkine levels. Importantly, TGF $\beta$  is known to  
761 regulate fractalkine expression, and we identified increased TGF $\beta$ 1 signaling among glial and vascular  
762 cell types, which likely acts as an upstream regulator of tissue remodeling after HX. While OPCs in the  
763 white matter became more abundant, newly formed OLs became less abundant, suggesting  
764 differentiation arrest, specifically in the transition from OPCs to newly formed OLs.

765 Further, we found that developing and mature OLs from the cortex and corpus callosum exhibited  
766 different cell states and responded differently to HX. At baseline, white matter OLs overall were more  
767 mature than cortical OLs (exhibiting higher OL maturation scores), and these levels did not change  
768 significantly following HX. Analysis of inter-lineage cell-cell communication revealed alterations in GAS6-  
769 TAM, EDN1-EDNRB, and fractalkine-CX3CR1 networks in the cortex that may play a direct role in  
770 promoting OPC differentiation and altering OL myelination capacity in the context of neonatal HX. In  
771 addition, we identify significant changes in the spatial organization of homeostatic astrocytes. Previous  
772 studies have shown that astrocyte-OL interactions are crucial in facilitating OPC differentiation into  
773 mature myelin-forming OL via a process orchestrated through the Nrf2 pathway (Molina-Gonzalez et al.,  
774 2023).

775 Importantly, we identified widespread changes in extracellular matrix components, including  
776 CSPGs, after HX. CSPGs contribute to the formation of perineuronal nets (PNNs) during postnatal  
777 development and play a role in the closure of the critical window of plasticity (Fawcett et al., 2019;  
778 Hensch, 2005). We observed that in most cell types in the cortex and corpus callosum, neonatal HX was

779 associated with increased expression of genes important for cell migration and projection guidance  
780 including ephrins and CSPGs. These signals may play an important role in coordinating the migration of  
781 injury-responsive cells such as immune cells and astrocytes, as well as migrating upper-layer excitatory  
782 neurons. Interestingly, we did find that the abundance and local organization of upper-layer excitatory  
783 neurons was disrupted by HX. However, it is unclear whether the upregulation of guidance cues such as  
784 CSPGs would help or hinder appropriate cell migration. Depletion of CSPGs in the adult brain by  
785 enzymatic degradation or genetic inhibition has been shown to promote plasticity (Lensjø et al., 2017;  
786 Reichelt et al., 2019; Willis et al., 2022). CSPGs can also act as potent inhibitors of myelination, axon  
787 guidance and regeneration, and other injury repair processes. Further work is needed to determine the  
788 clinical relevance of CSPGs in myelin recovery after neonatal WMI.

789 While most studies on neonatal WMI have focused on OL-lineage cells, our study underscores  
790 the complex and region-specific multicellular signaling that may support gliogenesis but also ultimately  
791 lead to impaired functional connectivity. Specifically, we found that endothelial cells, fibroblasts, and  
792 pericytes were major sources of signaling molecules, and that their phenotype changed dramatically  
793 following HX in a region-specific manner. Our findings imply that crosstalk signaling from vasculature-  
794 associated cells may be crucial for activating angiogenesis and forming adhesive interactions that  
795 maintain blood-brain barrier integrity and modulate permeability after HX exposure. Additionally, vascular  
796 cells may represent an important source of inflammatory ligands that promote microglial reactivity after  
797 neonatal HX. We also found that corpus callosum microglia may be less reactive than cortical microglia  
798 under NX and HX conditions, which contrasts with previous research in adult rodents and humans, that  
799 suggest that white matter microglia are more reactive to injury than gray matter microglia (Batchelor et  
800 al., 2008; van der Poel et al., 2019). As these earlier studies primarily involved adult and aged rodents,  
801 our findings reflect a different, developmental microglia state. Specifically, the heightened cortical  
802 microglial reactivity observed in our study may relate to their role in synapse refinement during brain  
803 development following HX exposure, although this requires further investigation.

804 An important strength of the present study is the use of MERFISH, which enables single cell-  
805 resolution spatial transcriptomics. Previous work on neonatal HX has focused largely on the corpus



806 callosum, but paracrine and non-cell autonomous mechanisms of recovery after neonatal brain injury are  
807 poorly understood. The present analysis spans most major anatomical brain regions and highlights  
808 regional variability in the vulnerability and response to injury. Nonetheless, there are several limitations to  
809 the present study. Firstly, the mouse model of chronic neonatal HX does not introduce inflammatory  
810 stimuli, which are often an important component of the encephalopathy of prematurity. Additionally, the  
811 sub-lethal chronic HX model employed does not fully replicate the intermittent hypoxic events  
812 experienced by many premature infants. Notably, the pattern of WMI in preterm infants has become less  
813 severe in the last two decades, and thus, cerebral dysmaturation may also be contributing to  
814 neurodevelopmental delays and impairments (Schneider and Miller, 2019). From a methodologic  
815 perspective, MERFISH requires segmentation of cell boundaries to assign transcripts to individual cells.  
816 We employed a machine learning algorithm and extensive manual curation, including stringent doublet  
817 elimination, to mitigate limitations of cell boundary identification. However, precise cell boundary  
818 identification remains an ongoing challenge for *in situ* spatial transcriptomics, and mis-segmentation may  
819 introduce false cell type assignment of gene expression. While our analysis was limited to a single time  
820 point, the objective of the study was to identify pathways critical for recovery and repair after neonatal  
821 HX. Finally, commercial MERFISH methods are presently limited to a finite number of genes, so  
822 additional changes at the level of the whole transcriptome were not captured.

823 Despite these limitations, this work presents an extensive spatially informed landscape of gene  
824 expression changes in an established mouse model of neonatal brain injury. We developed and  
825 employed a new approach to map physical cellular interactions using imaging-based spatial  
826 transcriptomics, which can be extended to other developmental and disease contexts. Our whole-brain  
827 analysis is a foundational resource for developmental WMI and for regenerative cellular communication.

828

829

830

831

832  
833  
834  
835  
836  
837  
838  
839  
840  
841  
842  
843  
844  
845  
846  
847  
848  
849  
850  
851  
852  
853  
854

**REFERENCES**

Aguirre A, Dupree JL, Mangin JM, Gallo V (2007) A functional role for EGFR signaling in myelination and remyelination. *Nat Neurosci* 10:990–1002.

Akhmetshina A, Palumbo K, Dees C, Bergmann C, Venalis P, Zerr P, Horn A, Kireva T, Beyer C, Zwerina J, Schneider H, Sadowski A, Riener M-O, MacDougald OA, Distler O, Schett G, Distler JHW (2012) Activation of canonical Wnt signalling is required for TGF- $\beta$ -mediated fibrosis. *Nat Commun* 3:735.

Allen WE, Blosser TR, Sullivan ZA, Dulac C, Zhuang X (2023) Molecular and spatial signatures of mouse brain aging at single-cell resolution. *Cell* 186:194-208.e18.

855 Argaw AT, Asp L, Zhang J, Navrazhina K, Pham T, Mariani JN, Mahase S, Dutta DJ, Seto J, Kramer EG,  
856 Ferrara N, Sofroniew MV, John GR (2012) Astrocyte-derived VEGF-A drives blood-brain barrier  
857 disruption in CNS inflammatory disease. *J Clin Invest* 122:2454–2468.

858 Back SA, Rosenberg PA (2014) Pathophysiology of glia in perinatal white matter injury. *Glia* 62:1790–  
859 1815.

860 Batchelor PE, Tan S, Wills TE, Porritt MJ, Howells DW (2008) Comparison of inflammation in the brain  
861 and spinal cord following mechanical injury. *J Neurotrauma* 25:1217–1225.

862 Battista D, Ferrari CC, Gage FH, Pitossi FJ (2006) Neurogenic niche modulation by activated microglia:  
863 transforming growth factor beta increases neurogenesis in the adult dentate gyrus. *Eur J Neurosci*  
864 23:83–93.

865 Bellver-Landete V, Bretheau F, Mailhot B, Vallières N, Lessard M, Janelle M-E, Vernoux N, Tremblay M-  
866 È, Fuehrmann T, Shoichet MS, Lacroix S (2019) Microglia are an essential component of the  
867 neuroprotective scar that forms after spinal cord injury. *Nat Commun* 10:518.

868 Bergles DE, Richardson WD (2015) Oligodendrocyte Development and Plasticity. *Cold Spring Harb*  
869 *Perspect Biol* 8:a020453.

870 Binder MD, Cate HS, Prieto AL, Kemper D, Butzkueven H, Gresle MM, Cipriani T, Jokubaitis VG,  
871 Carmeliet P, Kilpatrick TJ (2008) Gas6 deficiency increases oligodendrocyte loss and microglial  
872 activation in response to cuprizone-induced demyelination. *J Neurosci* 28:5195–5206.

873 Binder MD, Xiao J, Kemper D, Ma GZM, Murray SS, Kilpatrick TJ (2011) Gas6 increases myelination by  
874 oligodendrocytes and its deficiency delays recovery following cuprizone-induced demyelination.  
875 *PLoS One* 6:e17727.

876 Blencowe H, Cousens S, Chou D, Oestergaard M, Say L, Moller A-B, Kinney M, Lawn J, Born Too Soon  
877 Preterm Birth Action Group (2013a) Born too soon: the global epidemiology of 15 million preterm  
878 births. *Reprod Health* 10 Suppl 1:S2.

879 Blencowe H, Lee ACC, Cousens S, Bahalim A, Narwal R, Zhong N, Chou D, Say L, Modi N, Katz J, Vos  
880 T, Marlow N, Lawn JE (2013b) Preterm birth-associated neurodevelopmental impairment  
881 estimates at regional and global levels for 2010. *Pediatr Res* 74 Suppl 1:17–34.

882 Boche D, Gordon MN (2022) Diversity of transcriptomic microglial phenotypes in aging and Alzheimer's  
883 disease. *Alzheimers Dement* 18:360–376.

884 Bordiuk OL, Smith K, Morin PJ, Semenov MV (2014) Cell proliferation and neurogenesis in adult mouse  
885 brain. *PLoS One* 9:e111453.

886 Borrett MJ, Innes BT, Jeong D, Tahmasian N, Storer MA, Bader GD, Kaplan DR, Miller FD (2020) Single-  
887 Cell Profiling Shows Murine Forebrain Neural Stem Cells Reacquire a Developmental State when  
888 Activated for Adult Neurogenesis. *Cell Rep* 32:108022.

889 Brandi E, Torres-Garcia L, Svanbergsson A, Haikal C, Liu D, Li W, Li J-Y (2022) Brain region-specific  
890 microglial and astrocytic activation in response to systemic lipopolysaccharides exposure. *Front*  
891 *Aging Neurosci* 14:910988.

892 Bujalka H, Koenning M, Jackson S, Perreau VM, Pope B, Hay CM, Mitew S, Hill AF, Lu QR, Wegner M,  
893 Srinivasan R, Svaren J, Willingham M, Barres BA, Emery B (2013) MYRF is a membrane-  
894 associated transcription factor that autoproteolytically cleaves to directly activate myelin genes.  
895 *PLoS Biol* 11:e1001625.

896 Castillo-Ruiz A, Hite TA, Yakout DW, Rosen TJ, Forger NG (2020) Does Birth Trigger Cell Death in the  
897 Developing Brain? *eNeuro* 7:ENEURO.0517-19.2020.

898 Chavali M, Ulloa-Navas MJ, Pérez-Borredá P, Garcia-Verdugo JM, McQuillen PS, Huang EJ, Rowitch  
899 DH (2020) Wnt-Dependent Oligodendroglial-Endothelial Interactions Regulate White Matter  
900 Vascularization and Attenuate Injury. *Neuron* 108:1130-1145.e5.

901 Clarke LE, Liddelow SA, Chakraborty C, Münch AE, Heiman M, Barres BA (2018) Normal aging induces  
902 A1-like astrocyte reactivity. *Proc Natl Acad Sci U S A* 115:E1896–E1905.

903 Courtois-Cox S, Jones SL, Cichowski K (2008) Many roads lead to oncogene-induced senescence.  
904 *Oncogene* 27:2801–2809.

905 Crump C, Sundquist J, Sundquist K (2021) Preterm or Early Term Birth and Risk of Autism. *Pediatrics*  
906 148:e2020032300.

907 de Almeida MMA, Watson AES, Bibi S, Dittmann NL, Goodkey K, Sharafodinzadeh P, Galleguillos D,  
908 Nakhaei-Nejad M, Kosaraju J, Steinberg N, Wang BS, Footz T, Giuliani F, Wang J, Sipione S,

Edgar JM, Voronova A (2023) Fractalkine enhances oligodendrocyte regeneration and remyelination in a demyelination mouse model. *Stem Cell Reports* 18:519–533.

De Lucia C, Rinchon A, Olmos-Alonso A, Riecken K, Fehse B, Boche D, Perry VH, Gomez-Nicola D (2016) Microglia regulate hippocampal neurogenesis during chronic neurodegeneration. *Brain Behav Immun* 55:179–190.

De Marchis S, Fasolo A, Puche AC (2004) Subventricular zone-derived neuronal progenitors migrate into the subcortical forebrain of postnatal mice. *J Comp Neurol* 476:290–300.

Dizon MLV, Maa T, Kessler JA (2011) The bone morphogenetic protein antagonist noggin protects white matter after perinatal hypoxia-ischemia. *Neurobiol Dis* 42:318–326.

Dries R, Zhu Q, Dong R, Eng C-HL, Li H, Liu K, Fu Y, Zhao T, Sarkar A, Bao F, George RE, Pierson N, Cai L, Yuan G-C (2021) Giotto: a toolbox for integrative analysis and visualization of spatial expression data. *Genome Biol* 22:78.

Dyck SM, Karimi-Abdolrezaee S (2015) Chondroitin sulfate proteoglycans: Key modulators in the developing and pathologic central nervous system. *Exp Neurol* 269:169–187.

Fagel DM, Ganat Y, Silbereis J, Ebbitt T, Stewart W, Zhang H, Ment LR, Vaccarino FM (2006) Cortical neurogenesis enhanced by chronic perinatal hypoxia. *Exp Neurol* 199:77–91.

Fawcett JW, Ohashi T, Pizzorusso T (2019) The roles of perineuronal nets and the perinodal extracellular matrix in neuronal function. *Nat Rev Neurosci* 20:451–465.

Finak G, McDavid A, Yajima M, Deng J, Gersuk V, Shalek AK, Slichter CK, Miller HW, McElrath MJ, Prlic M, Linsley PS, Gottardo R (2015) MAST: a flexible statistical framework for assessing transcriptional changes and characterizing heterogeneity in single-cell RNA sequencing data. *Genome Biol* 16:278.

Floriddia EM, Lourenço T, Zhang S, van Bruggen D, Hilscher MM, Kukanja P, Gonçalves Dos Santos JP, Altınkök M, Yokota C, Llorens-Bobadilla E, Mulinyawe SB, Grãos M, Sun LO, Frisén J, Nilsson M, Castelo-Branco G (2020) Distinct oligodendrocyte populations have spatial preference and different responses to spinal cord injury. *Nat Commun* 11:5860.

935 Forbes TA, Goldstein EZ, Dupree JL, Jablonska B, Scafidi J, Adams KL, Imamura Y, Hashimoto-Torii K,  
936 Gallo V (2020) Environmental enrichment ameliorates perinatal brain injury and promotes  
937 functional white matter recovery. *Nat Commun* 11:964.

938 Fujioka T, Kaneko N, Ajioka I, Nakaguchi K, Omata T, Ohba H, Fässler R, García-Verdugo JM, Sekiguchi  
939 K, Matsukawa N, Sawamoto K (2017)  $\beta$ 1 integrin signaling promotes neuronal migration along  
940 vascular scaffolds in the post-stroke brain. *EBioMedicine* 16:195–203.

941 Fumagalli M, Daniele S, Lecca D, Lee PR, Parravicini C, Fields RD, Rosa P, Antonucci F, Verderio C,  
942 Trincavelli ML, Bramanti P, Martini C, Abbracchio MP (2011) Phenotypic changes, signaling  
943 pathway, and functional correlates of GPR17-expressing neural precursor cells during  
944 oligodendrocyte differentiation. *J Biol Chem* 286:10593–10604.

945 Furusho M, Dupree JL, Nave K-A, Bansal R (2012) Fibroblast growth factor receptor signaling in  
946 oligodendrocytes regulates myelin sheath thickness. *J Neurosci* 32:6631–6641.

947 Furusho M, Roulois AJ, Franklin RJM, Bansal R (2015) Fibroblast growth factor signaling in  
948 oligodendrocyte-lineage cells facilitates recovery of chronically demyelinated lesions but is  
949 redundant in acute lesions. *Glia* 63:1714–1728.

950 Gaborieau E, Hurtado-Chong A, Fernández M, Azim K, Raineteau O (2018) A dual role for the  
951 transcription factor Sp8 in postnatal neurogenesis. *Sci Rep* 8:14560.

952 Gerber YN, Saint-Martin GP, Bringuier CM, Bartolami S, Goze-Bac C, Noristani HN, Perrin FE (2018)  
953 CSF1R Inhibition Reduces Microglia Proliferation, Promotes Tissue Preservation and Improves  
954 Motor Recovery After Spinal Cord Injury. *Front Cell Neurosci* 12:368.

955 Guo F, Wang Y (2023) TCF7L2, a nuclear marker that labels premyelinating oligodendrocytes and  
956 promotes oligodendroglial lineage progression. *Glia* 71:143–154.

957 Hammond TR et al. (2019) Single-Cell RNA Sequencing of Microglia throughout the Mouse Lifespan and  
958 in the Injured Brain Reveals Complex Cell-State Changes. *Immunity* 50:253-271.e6.

959 Hammond TR, McEllin B, Morton PD, Raymond M, Dupree J, Gallo V (2015) Endothelin-B Receptor  
960 Activation in Astrocytes Regulates the Rate of Oligodendrocyte Regeneration during  
961 Remyelination. *Cell Rep* 13:2090–2097.

962 Harboe M, Torvund-Jensen J, Kjaer-Sorensen K, Laursen LS (2018) Ephrin-A1-EphA4 signaling  
 963 negatively regulates myelination in the central nervous system. *Glia* 66:934–950.  
 964 Hensch TK (2005) Critical period plasticity in local cortical circuits. *Nat Rev Neurosci* 6:877–888.  
 965 Herrero-Navarro Á, Puche-Aroca L, Moreno-Juan V, Sempere-Ferrández A, Espinosa A, Susín R,  
 966 Torres-Masjoan L, Leyva-Díaz E, Karow M, Figueres-Oñate M, López-Mascaraque L, López-  
 967 Atalaya JP, Berninger B, López-Bendito G (2021) Astrocytes and neurons share region-specific  
 968 transcriptional signatures that confer regional identity to neuronal reprogramming. *Sci Adv*  
 969 7:eabe8978.  
 970 Hilscher MM, Langseth CM, Kukanja P, Yokota C, Nilsson M, Castelo-Branco G (2022) Spatial and  
 971 temporal heterogeneity in the lineage progression of fine oligodendrocyte subtypes. *BMC Biol*  
 972 20:122.  
 973 Hirvonen M, Ojala R, Korhonen P, Haataja P, Eriksson K, Gissler M, Luukkaala T, Tammela O (2017)  
 974 The incidence and risk factors of epilepsy in children born preterm: A nationwide register study.  
 975 *Epilepsy Res* 138:32–38.  
 976 Jablonska B, Adams KL, Kratimenos P, Li Z, Strickland E, Haydar TF, Kusch K, Nave K-A, Gallo V  
 977 (2022) Sirt2 promotes white matter oligodendrogenesis during development and in models of  
 978 neonatal hypoxia. *Nat Commun* 13:4771.  
 979 Jin S, Plikus MV, Nie Q (2023) CellChat for systematic analysis of cell-cell communication from single-  
 980 cell and spatially resolved transcriptomics.  
 981 Joglekar A et al. (2021) A spatially resolved brain region- and cell type-specific isoform atlas of the  
 982 postnatal mouse brain. *Nat Commun* 12:463.  
 983 Kirby L, Jin J, Cardona JG, Smith MD, Martin KA, Wang J, Strasburger H, Herbst L, Alexis M, Karnell J,  
 984 Davidson T, Dutta R, Goverman J, Bergles D, Calabresi PA (2019) Oligodendrocyte precursor  
 985 cells present antigen and are cytotoxic targets in inflammatory demyelination. *Nat Commun*  
 986 10:3887.  
 987 Klimaschewski L, Claus P (2021) Fibroblast Growth Factor Signalling in the Diseased Nervous System.  
 988 *Mol Neurobiol* 58:3884–3902.

989 Knox EG, Aburto MR, Clarke G, Cryan JF, O'Driscoll CM (2022) The blood-brain barrier in aging and  
990 neurodegeneration. *Mol Psychiatry* 27:2659–2673.

991 Koufi F-D, Neri I, Ramazzotti G, Rusciano I, Mongiorgi S, Marvi MV, Fazio A, Shin M, Kosodo Y, Cani I,  
992 Giorgio E, Cortelli P, Manzoli L, Ratti S (2023) Lamin B1 as a key modulator of the developing  
993 and aging brain. *Front Cell Neurosci* 17:1263310.

994 Kucukdereli H, Allen NJ, Lee AT, Feng A, Ozlu MI, Conatser LM, Chakraborty C, Workman G, Weaver  
995 M, Sage EH, Barres BA, Eroglu C (2011) Control of excitatory CNS synaptogenesis by astrocyte-  
996 secreted proteins Hevin and SPARC. *Proc Natl Acad Sci U S A* 108:E440-449.

997 Lensjø KK, Lepperød ME, Dick G, Hafting T, Fyhn M (2017) Removal of Perineuronal Nets Unlocks  
998 Juvenile Plasticity Through Network Mechanisms of Decreased Inhibition and Increased Gamma  
999 Activity. *J Neurosci* 37:1269–1283.

1000 Li W, Chen Zhigang, Chin I, Chen Zhong, Dai H (2018) The Role of VE-cadherin in Blood-brain Barrier  
1001 Integrity Under Central Nervous System Pathological Conditions. *Curr Neuropharmacol* 16:1375–  
1002 1384.

1003 Li Y, Su P, Chen Y, Nie J, Yuan T-F, Wong AH, Liu F (2022) The Eph receptor A4 plays a role in  
1004 demyelination and depression-related behavior. *J Clin Invest* 132:e152187.

1005 Liddelow SA et al. (2017) Neurotoxic reactive astrocytes are induced by activated microglia. *Nature*  
1006 541:481–487.

1007 Luo F, Wang J, Zhang Z, You Z, Bedolla A, Okwubido-Williams F, Huang LF, Silver J, Luo Y (2022)  
1008 Inhibition of CSPG receptor PTP $\sigma$  promotes migration of newly born neuroblasts, axonal  
1009 sprouting, and recovery from stroke. *Cell Rep* 40:111137.

1010 Makwana M, Jones LL, Cuthill D, Heuer H, Bohatschek M, Hristova M, Friedrichsen S, Ormsby I,  
1011 Bueringer D, Koppius A, Bauer K, Doetschman T, Raivich G (2007) Endogenous transforming  
1012 growth factor beta 1 suppresses inflammation and promotes survival in adult CNS. *J Neurosci*  
1013 27:11201–11213.

1014 Marques S et al. (2016) Oligodendrocyte heterogeneity in the mouse juvenile and adult central nervous  
1015 system. *Science* 352:1326–1329.



1016 Matusova Z, Hol EM, Pekny M, Kubista M, Valihrach L (2023) Reactive astrogliosis in the era of single-  
1017 cell transcriptomics. *Front Cell Neurosci* 17:1173200.

1018 Mercurio D, Fumagalli S, Schafer MK-H, Pedragosa J, Ngassam LDC, Wilhelmi V, Winterberg S, Planas  
1019 AM, Weihe E, De Simoni M-G (2022) Protein Expression of the Microglial Marker Tmem119  
1020 Decreases in Association With Morphological Changes and Location in a Mouse Model of  
1021 Traumatic Brain Injury. *Front Cell Neurosci* 16:820127.

1022 Miyamoto N, Maki T, Shindo A, Liang AC, Maeda M, Egawa N, Itoh K, Lo EK, Lok J, Ihara M, Arai K  
1023 (2015) Astrocytes Promote Oligodendrogenesis after White Matter Damage via Brain-Derived  
1024 Neurotrophic Factor. *J Neurosci* 35:14002–14008.

1025 Molina-Gonzalez I et al. (2023) Astrocyte-oligodendrocyte interaction regulates central nervous system  
1026 regeneration. *Nat Commun* 14:3372.

1027 Nicaise AM, Wagstaff LJ, Willis CM, Paisie C, Chandok H, Robson P, Fossati V, Williams A, Crocker SJ  
1028 (2019) Cellular senescence in progenitor cells contributes to diminished remyelination potential in  
1029 progressive multiple sclerosis. *Proceedings of the National Academy of Sciences* 116:9030–9039.

1030 Osterhout DJ, Wolven A, Wolf RM, Resh MD, Chao MV (1999) Morphological differentiation of  
1031 oligodendrocytes requires activation of Fyn tyrosine kinase. *J Cell Biol* 145:1209–1218.

1032 Pachitariu M, Stringer C (2022) Cellpose 2.0: how to train your own model. *Nat Methods* 19:1634–1641.

1033 Palla G, Spitzer H, Klein M, Fischer D, Schaar AC, Kuemmerle LB, Rybakov S, Ibarra IL, Holmberg O,  
1034 Virshup I, Lotfollahi M, Richter S, Theis FJ (2022) Squidpy: a scalable framework for spatial omics  
1035 analysis. *Nat Methods* 19:171–178.

1036 Paolicelli RC et al. (2022) Microglia states and nomenclature: A field at its crossroads. *Neuron* 110:3458–  
1037 3483.

1038 Pfisterer U, Khodosevich K (2017) Neuronal survival in the brain: neuron type-specific mechanisms. *Cell*  
1039 *Death Dis* 8:e2643.

1040 Reichelt AC, Hare DJ, Bussey TJ, Saksida LM (2019) Perineuronal Nets: Plasticity, Protection, and  
1041 Therapeutic Potential. *Trends Neurosci* 42:458–470.

1042 Renz P, Surbek D, Haesler V, Tscherrig V, Huang EJ, Chavali M, Liddelow S, Rowitch D, Schoeberlein  
1043 A, Lutz AB (2022) Silencing neuroinflammatory reactive astrocyte activating factors ameliorates  
1044 disease outcomes in perinatal white matter injury.

1045 Ribeiro Xavier AL, Kress BT, Goldman SA, Lacerda de Menezes JR, Nedergaard M (2015) A Distinct  
1046 Population of Microglia Supports Adult Neurogenesis in the Subventricular Zone. *J Neurosci*  
1047 35:11848–11861.

1048 Ridderstad Wollberg A, Ericsson-Dahlstrand A, Juréus A, Ekerot P, Simon S, Nilsson M, Wiklund S-J,  
1049 Berg A-L, Ferm M, Sunnemark D, Johansson R (2014) Pharmacological inhibition of the  
1050 chemokine receptor CX3CR1 attenuates disease in a chronic-relapsing rat model for multiple  
1051 sclerosis. *Proc Natl Acad Sci U S A* 111:5409–5414.

1052 Rommel A-S, James S-N, McLoughlin G, Brandeis D, Banaschewski T, Asherson P, Kuntsi J (2017)  
1053 Association of Preterm Birth With Attention-Deficit/Hyperactivity Disorder-Like and Wider-Ranging  
1054 Neurophysiological Impairments of Attention and Inhibition. *J Am Acad Child Adolesc Psychiatry*  
1055 56:40–50.

1056 Safaiyan S, Kannaiyan N, Snaidero N, Brioschi S, Biber K, Yona S, Edinger AL, Jung S, Rossner MJ,  
1057 Simons M (2016) Age-related myelin degradation burdens the clearance function of microglia  
1058 during aging. *Nat Neurosci* 19:995–998.

1059 Salmaso N, Jablonska B, Scafidi J, Vaccarino FM, Gallo V (2014) Neurobiology of premature brain injury.  
1060 *Nat Neurosci* 17:341–346.

1061 Sathyanesan A, Kundu S, Abbah J, Gallo V (2018) Neonatal brain injury causes cerebellar learning  
1062 deficits and Purkinje cell dysfunction. *Nat Commun* 9:3235.

1063 Schneider J, Miller SP (2019) Preterm brain Injury: White matter injury. *Handb Clin Neurol* 162:155–172.

1064 Semple BD, Blomgren K, Gimlin K, Ferriero DM, Noble-Haeusslein LJ (2013) Brain development in  
1065 rodents and humans: Identifying benchmarks of maturation and vulnerability to injury across  
1066 species. *Prog Neurobiol* 106–107:1–16.

1067 Siebert JR, Conta Steencken A, Osterhout DJ (2014) Chondroitin sulfate proteoglycans in the nervous  
1068 system: inhibitors to repair. *Biomed Res Int* 2014:845323.

1069 Spitzer SO, Sitnikov S, Kamen Y, Evans KA, Kronenberg-Versteeg D, Dietmann S, de Faria O, Agathou  
 1070 S, Káradóttir RT (2019) Oligodendrocyte Progenitor Cells Become Regionally Diverse and  
 1071 Heterogeneous with Age. *Neuron* 101:459-471.e5.

1072 Stogsdill JA, Kim K, Binan L, Farhi SL, Levin JZ, Arlotta P (2022) Pyramidal neuron subtype diversity  
 1073 governs microglia states in the neocortex. *Nature* 608:750–756.

1074 Takeuchi A, Takahashi Y, Iida K, Hosokawa M, Irie K, Ito M, Brown JB, Ohno K, Nakashima K, Hagiwara  
 1075 M (2020) Identification of Qk as a Glial Precursor Cell Marker that Governs the Fate Specification  
 1076 of Neural Stem Cells to a Glial Cell Lineage. *Stem Cell Reports* 15:883–897.

1077 Tan Y-L, Yuan Y, Tian L (2020) Microglial regional heterogeneity and its role in the brain. *Mol Psychiatry*  
 1078 25:351–367.

1079 Ułanska-Poutanen J, Mieczkowski J, Zhao C, Konarzewska K, Kaza B, Pohl HB, Bugajski L, Kaminska  
 1080 B, Franklin RJ, Zawadzka M (2018) Injury-induced perivascular niche supports alternative  
 1081 differentiation of adult rodent CNS progenitor cells. *Elife* 7:e30325.

1082 van der Poel M, Ulas T, Mizze MR, Hsiao C-C, Miedema SSM, Adelia null, Schuurman KG, Helder B,  
 1083 Tas SW, Schultze JL, Hamann J, Huitinga I (2019) Transcriptional profiling of human microglia  
 1084 reveals grey-white matter heterogeneity and multiple sclerosis-associated changes. *Nat Commun*  
 1085 10:1139.

1086 Varela-Nallar L, Rojas-Abalos M, Abbott AC, Moya EA, Iturriaga R, Inestrosa NC (2014) Chronic hypoxia  
 1087 induces the activation of the Wnt/ $\beta$ -catenin signaling pathway and stimulates hippocampal  
 1088 neurogenesis in wild-type and APP<sup>swe</sup>-PS1 $\Delta$ E9 transgenic mice in vivo. *Front Cell Neurosci*  
 1089 8:17.

1090 Wahane S, Zhou Xianxiao, Zhou Xiang, Guo L, Friedl M-S, Kluge M, Ramakrishnan A, Shen L, Friedel  
 1091 CC, Zhang B, Friedel RH, Zou H (2021) Diversified transcriptional responses of myeloid and glial  
 1092 cells in spinal cord injury shaped by HDAC3 activity. *Sci Adv* 7:eabd8811.

1093 Willis A, Pratt JA, Morris BJ (2022) Enzymatic Degradation of Cortical Perineuronal Nets Reverses  
 1094 GABAergic Interneuron Maturation. *Mol Neurobiol* 59:2874–2893.

1095 Wu M, Hernandez M, Shen S, Sabo JK, Kelkar D, Wang J, O'Leary R, Phillips GR, Cate HS, Casaccia P  
1096 (2012) Differential modulation of the oligodendrocyte transcriptome by sonic hedgehog and bone  
1097 morphogenetic protein 4 via opposing effects on histone acetylation. *J Neurosci* 32:6651–6664.

1098 Yuzwa SA, Borrett MJ, Innes BT, Voronova A, Ketela T, Kaplan DR, Bader GD, Miller FD (2017)  
1099 Developmental Emergence of Adult Neural Stem Cells as Revealed by Single-Cell Transcriptional  
1100 Profiling. *Cell Rep* 21:3970–3986.

1101 Zamanian JL, Xu L, Foo LC, Nouri N, Zhou L, Giffard RG, Barres BA (2012) Genomic analysis of reactive  
1102 astrogliosis. *J Neurosci* 32:6391–6410.

1103 Zhang M, Eichhorn SW, Zingg B, Yao Z, Cotter K, Zeng H, Dong H, Zhuang X (2021) Spatially resolved  
1104 cell atlas of the mouse primary motor cortex by MERFISH. *Nature* 598:137–143.

1105 Zhang M, Pan X, Jung W, Halpern AR, Eichhorn SW, Lei Z, Cohen L, Smith KA, Tasic B, Yao Z, Zeng H,  
1106 Zhuang X (2023) Molecularly defined and spatially resolved cell atlas of the whole mouse brain.  
1107 *Nature* 624:343–354.

1108 Zhou Z-L, Xie H, Tian X-B, Xu H-L, Li W, Yao S, Zhang H (2023) Microglial depletion impairs glial scar  
1109 formation and aggravates inflammation partly by inhibiting STAT3 phosphorylation in astrocytes  
1110 after spinal cord injury. *Neural Regen Res* 18:1325–1331.

1122 **LEGENDS**

1123 **Figure 1: Multiplexed error-robust fluorescent *in situ* hybridization (MERFISH) sequencing**  
1124 **identifies all major cell types and anatomical regions of the postnatal murine brain. (A)** Schematic  
1125 representation of the HX paradigm, tissue harvesting, tissue processing, quality control, and downstream  
1126 data analysis approach applied to the MERFISH dataset. Tissue was harvested and processed for  
1127 postnatal day 21 (P21) HX and NX mice ( $n = 3$  male mice per condition). The MERFISH probe set used  
1128 in this study targeted a curated panel of genes listed in Extended Data Table 1-1. MERFISH-derived  
1129 spatial map displaying the **(B)** major anatomical regions outlined during sample processing steps, and  
1130 **(C)** a select set of genes used to identify and outline the anatomical regions utilized in downstream data  
1131 analysis. Areas of the brain are colored according to their anatomical region or major identifying gene.

1132 **Figure 2: Cell type classification and spatial distribution in the P21 mouse cortex.** Profiling of non-  
1133 neuronal **(A-B)** and neuronal **(C-D)** cell types in the cortex for a total of 668,947 cells. Transcriptomic  
1134 profiling for corpus callosum and subventricular zone (SVZ) cells is shown in Figure 3, and profiling of  
1135 septum, caudate putamen (CP), anterior commissure (ACo), and septal white matter tracts (SWM) cells  
1136 is shown in Extended Data Figure 2-1. Quality control metrics for each replicate are shown in Extended  
1137 Data Figure 2-2. **(A)** Violin plots showing gene expression patterns of non-neuronal Cell Subtypes.  
1138 UMAP visualization of **(B)** non-neuronal cells colored by Cell Subtype as in (A), and **(C)** neuronal cells  
1139 colored by Cell Subtype as in (D). UMAP plots are generated from combined replicates across NX and  
1140 HX conditions. Each dot represents a single cell, and cells are grouped with a solid line into major Cell  
1141 Types. Each major Cell Type group was subsetted and clustered independently to allow identification of  
1142 Cell Subtypes. UMAP visualizations of each Cell Type dataset, colored by Cell Subtype, are shown in  
1143 Extended Data Figure 2-3. **(D)** Violin plot showing gene expression patterns of neuronal Cell Subtypes.  
1144 (A, D) Violin plots show several key canonical marker genes used for cluster identification. The width of  
1145 the violin corresponds to the proportion of nuclei expressing the indicated gene, and the color of the violin  
1146 corresponds to the Cell Subtype. Abbreviations for cell types are as follows: Exc: excitatory neuron, Int:  
1147 interneuron, Exc-1,2,3: cortical layers I-III excitatory neurons, Exc-2,3: cortical layers II-III excitatory  
1148 neurons, Exc-2,3,4: cortical layers II-IV excitatory neurons, Exc-2,3,4,P: cortical layers II-IV excitatory

neurons and piriform neurons, Exc-5: cortical layer V excitatory neurons, Exc-5,6: cortical layers V-VI excitatory neurons, Exc-6b,P2,3: cortical layer VIb excitatory neurons and piriform neurons, Exc-6b,SP: cortical layer VI excitatory neurons and subplate neurons, Piri: piriform neurons, SP: subplate neurons, Vasc: vascular cell, OL: oligodendrocyte-lineage cell, Astro: astrocyte, Micro: microglia, OL-immat: immature oligodendrocyte, OL-mat: mature oligodendrocyte, OL-new: newly-formed oligodendrocyte, OPC: oligodendrocyte precursor cell, Astro-hom: homeostatic astrocyte, Astro-react: reactive astrocyte, Micro-hom: homeostatic microglia, Micro-react: reactive microglia, Endo: endothelial cell, Fibro: fibroblast, Peri: pericyte. Spatial plots displaying the distribution of **(E)** OL-lineage cells, **(F)** astrocytes, **(G)** microglia, **(H)** vascular cells, **(I)** interneurons, and **(J)** excitatory neurons. Spatial plots are colored by Cell Subtype, dotted lines demarcate the cortex, and labels include deep part of cortex, “d”, superficial part of cortex, “s”, and meninges, “m”. Bar plots displaying the proportion of **(K)** neuronal, **(L)** OL-lineage, and **(M)** non-neuronal Cell Subtypes in the cortex of HX versus NX mice. The x-axis displays all major Cell Types and Cell Subtypes profiled through MERFISH. Data obtained from  $n = 3$  male biological replicates per condition. Bars represent the average values for each condition, and dots represent the average values for each mouse per condition. Significance is determined using the two-tailed Student’s t-test. \*p-value < 0.05; \*\*p-value < 0.01. Comparisons not labeled with asterisks are not significant. Error bars represent the average  $\pm$  1 standard deviation. Each bar is labeled by Cell Subtype as previously defined.

**Figure 3: Cell type classification and spatial distribution in the P21 mouse SVZ and corpus callosum reveals arrested OL differentiation in the corpus callosum following neonatal hypoxia.**

**(A)** UMAP visualization of all corpus callosum cells, totaling 8,708 cells. UMAP plots are generated from combined replicates across NX and HX conditions. Quality control metrics for each replicate are shown in Extended Data Figure 2-2. Each dot represents a single cell, and cells are grouped with a solid line into major Cell Types as follows: Astro: astrocyte, Micro: microglia, OL: oligodendrocyte, Vasc: vascular. Each major Cell Type group was subsetted and clustered independently to allow identification of Cell Subtypes. UMAP visualizations of each Cell Type dataset, colored by Cell SubType, are shown in Extended Data Figure 3-1. **(B)** Violin plot showing gene expression patterns of Cell Subtypes identified in

the corpus callosum with several key canonical marker genes used for cluster identification. The width of the violin corresponds to the proportion of cells expressing the indicated gene, and the color of the violin corresponds to the cell subtype. Each column is labeled by Cell Subtype as previously defined. **(C')** Spatial plot displaying the distribution of Cell Types in the CC. **(C'')** Zoomed view of the panel delineated in C'. **(D)** UMAP visualization of all SVZ cells, totaling 10,754 cells. UMAP plot is generated from combined replicates across NX and HX conditions. Quality control metrics for each replicate are shown in Extended Data Figure 2-2. Each cluster is colored by cell type and are labeled by cell type, with all NSCs labeled together and all neuroblasts labeled together, as follows: Epen: ependymal cell, TAP: transit amplifying progenitor, NB: neuroblast, NB-OB: olfactory bulb neuroblast, NSC: neural stem cell, NSC (dors): dorsal neural stem cell, NSC (sept): septal neural stem cell, NSC (vent): ventral neural stem cell. **(E)** Violin plot showing gene expression patterns of Cell Subtypes identified in the SVZ with several key canonical marker genes used for cluster identification. The width of the violin corresponds to the proportion of cells expressing the indicated gene, and the color of the violin corresponds to the cell subtype. Each column is labeled by Cell Subtype as previously defined. Bar plots displaying the proportion of **(F)** Cell Subtypes **(G)** OL-lineage Cell Subtypes of HX versus NX mice. **(H)** Bar plot displaying the proportion of Cell Subtypes in the SVZ of HX versus NX mice. The x-axis displays all major Cell Subtypes profiled through MERFISH. Data obtained from  $n = 3$  male biological replicates per condition. Bars represent the average values for each condition, and dots represent the average values for each mouse per condition. Error bars represent the average  $\pm 1$  standard deviation. Each bar is labeled by cell subtype as previously defined. **(I)** Spatial plot displaying the distribution of Cell Subtypes in the SVZ. For (C) and (I), the label "d" denotes dorsal, "v" denotes ventral, and "s" denotes septal.

**Figure 4: Neonatal hypoxia alters local spatial proximity between select Cell Type pairs across brain regions.** Differential proximities between cell type pairs (heatmaps) in the **(A)** cortex, **(B)** corpus callosum, and **(C)** SVZ. For cortex and corpus callosum, Cell Subtype classification was used. Positive scores (purple) indicate an increased proportion of the surrounding cell type (columns, x-axis) in proximity of the center cell type (rows, y-axis) in HX relative to NX, whereas negative scores (green) indicate a decrease. Grey indicates not enough non-zero data was present for the respective cell type

pair. Significant ( $FDR < 0.05$ ) relationships are denoted with an asterisk. Exemplar spatial plots (right panels) indicate the distribution of select center and surround cell types between NX (top) and HX (bottom) in **(D)** cortex, **(E)** corpus callosum, and **(F)** SVZ. The outer circles in the spatial plots correspond to the radius used to calculate the differential proximities in **(A-C)** and have been normalized to reflect the median cellular distances per sample. Violin plots (left panels) show the counts of the surrounding cell type in proximity to every central cell across the sample corresponding to the spatial plot (not just the sample area shown). P-values for t-tests are shown.

**Figure 5: Differential gene expression analysis finds transcriptionally distinct cellular subpopulations in the HX brain. (A-C)** Strip plots displaying DEGs between P21 HX and NX mice. Each dot represents a DEG: colored dots represent significant genes ( $FDR < 0.05$ ) per cell type, gray dots represent non-significant genes ( $FDR > 0.05$ ). The x-axis displays all major cell types across the **(A)** cortex, **(B)** corpus callosum, and **(C)** SVZ regions profiled through MERFISH analysis. Data obtained from  $n = 3$  biological replicates per condition. **(D-F)** UpSet plots displaying the number of unique and shared DEGs across cell types in the **(D)** cortex, **(E)** corpus callosum, and **(F)** SVZ. Unique genes are colored based on cell type, and genes shared between two or three cell types are indicated by black dots connected by lines according to shared origins. The horizontal histogram indicates the number of significant DEGs for each cell type, and the vertical barplots show the number of significant DEGs ( $FDR < 0.05$ ) specific to one, two, or three cell types. **(G)** Differential gene expression comparison of HX and NX in each region (cortex, corpus callosum, and SVZ) for signaling genes across Cell Types. **(H)** Representative images of NCAN immunofluorescence stained P21 NX and HX cortices from coronal slices. The cortex of each slice was manually segmented into three approximately equidistant regions encompassing the superficial (supr.) cortical layers, middle cortical layers, and deep cortical layers. Dashed lines demarcate the corpus callosum, "CC". **(I-J)** Average positive fluorescence intensity of NCAN across the area of the **(I)** entire cortex and **(J)** each of the three segmented regions in **(H)**. **(K-L)** Differential gene expression comparison of HX and NX in each region (cortex, corpus callosum, and SVZ) for **(K)** OL state genes across all OL-lineage cells (from Cell Type) and Cell Subtypes within the OL-lineage **(L)** astrocyte reactivity genes across all astrocytes (Astro from Cell Type) and Cell Subtypes



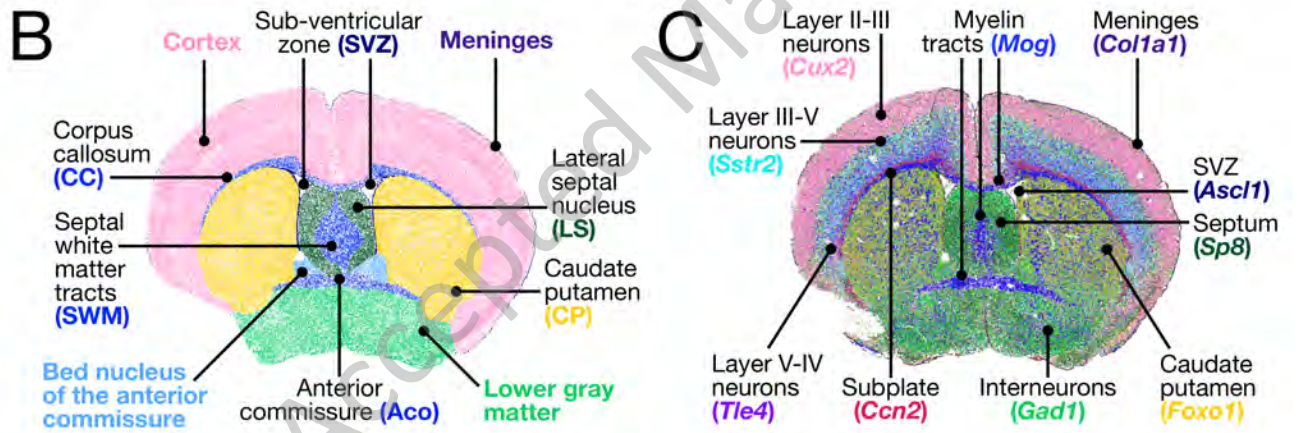
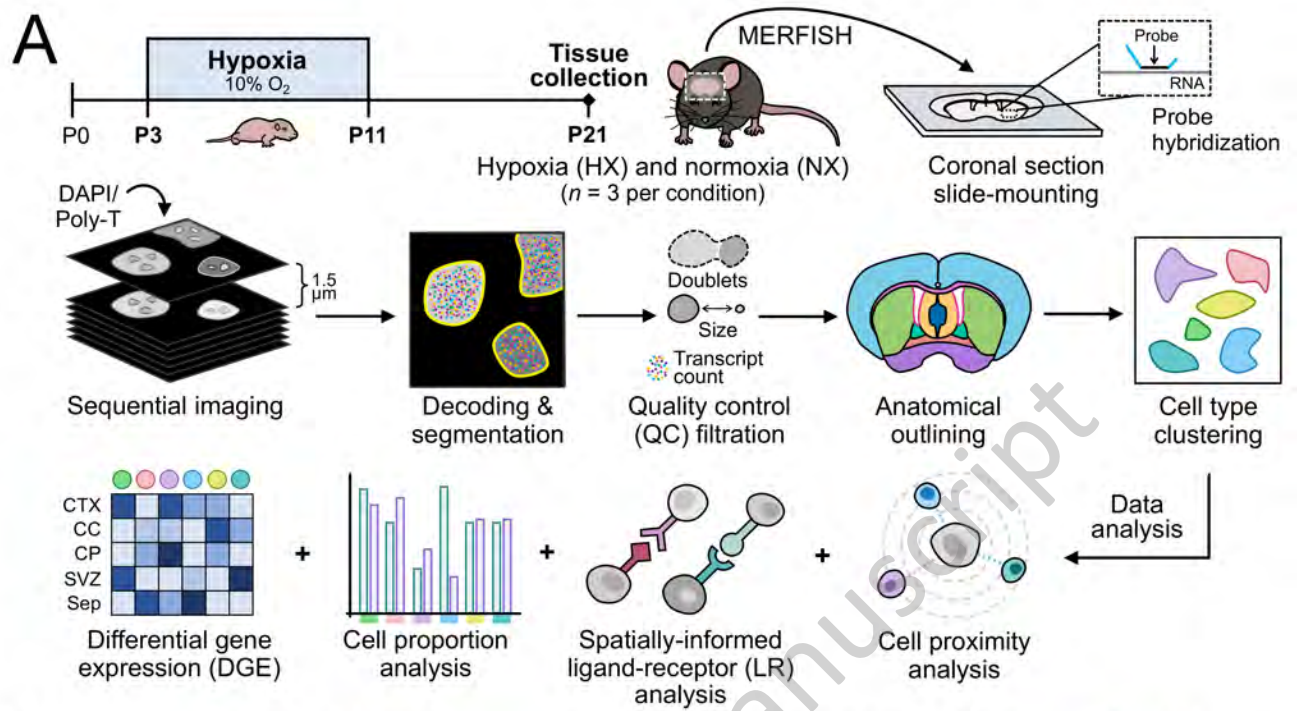
1230 within astrocytes, and **(M)** microglia reactivity genes across all microglia (Micro from Cell Type) and Cell  
1231 Subtypes within microglia. Genes in **(K)** are grouped and labeled according to the signaling pathway or  
1232 function that they participate in. Cortex and corpus callosum data in (A, B, D, E, G) display Cell Type  
1233 information, and in (K, L) display both Cell Type and Cell Subtype information. Only significant genes are  
1234 shown. Colors represent average  $\log_2(\text{FC})$  as per legend. Differential gene expression results comparing  
1235 signaling genes from one anatomical region to another within the NX brain are shown in Extended Data  
1236 Figure 5-1. Full differential gene expression results, including genes not shown here, are shown in  
1237 Extended Data Table 5-1.

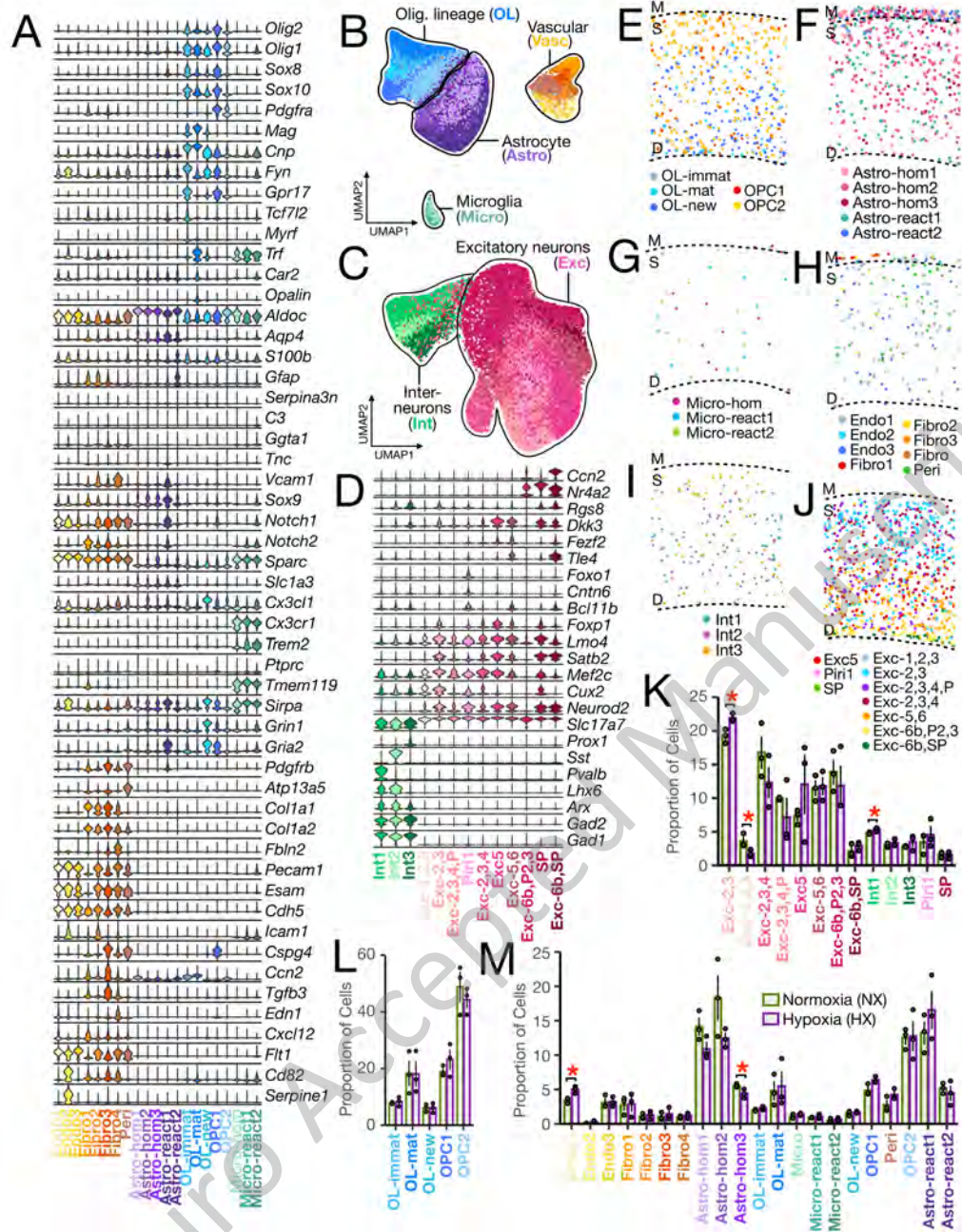
1238 **Figure 6: Cell subtypes exhibit discrete cell-cell signaling networks in the brain of mice exposed**  
1239 **to neonatal hypoxia.** Chord diagrams of predicted intra-lineage cell-cell communication pathways that  
1240 are upregulated in the **(A)** SVZ, **(B)** corpus callosum, and **(C)** cortex of HX versus NX mice. Chord  
1241 diagrams of predicted inter-lineage cell-cell communication pathways that are upregulated in the **(D)**  
1242 SVZ, **(E)** corpus callosum, and **(F)** cortex of HX versus NX mice. Cell Subtype identity of the ligand is  
1243 indicated in the outermost edge of the diagram, while the Cell Subtype identity of the receptor is indicated  
1244 by the internal ring. Encoding gene symbols are used to represent predicted interactions of their protein  
1245 products. Colored arrows indicate the specific ligand-receptor (LR) pairs and are colored according to the  
1246 outgoing ligand signal. For all chord diagrams, only significant ligand and receptor interactions are plotted  
1247 ( $p < 0.05$ ). Full results are shown in Extended Data Table 6-1.

1248 **Figure 7: Cell state changes of OL-lineage cells, astrocytes, and microglia across anatomical**  
1249 **regions and following neonatal hypoxia exposure.** Dotplots displaying differential gene expression  
1250 results of OL-state (OL genesis and OL maturation) genes comparing all OL-lineage cells (Cell Type) and  
1251 Cell Subtypes within NX and HX between **(A)** SVZ and deep cortex, **(B)** SVZ and upper cortex, **(C)** upper  
1252 and deep cortex, **(D)** corpus callosum (CC in all panels) and deep cortex, and **(E)** corpus callosum and  
1253 upper cortex. Violin-boxplots showing OL genesis state score in **(F)** newly-formed OLs and **(G)** OPCs,  
1254 and OL maturation score of **(H)** all OLs, **(I)** immature OLs, and **(J)** mature OLs, split and colored by  
1255 condition across the SVZ, corpus callosum, and cortex. Dotplots displaying differential gene expression  
1256 results of astrocyte reactivity genes comparing all astrocyte Cell Types and Cell Subtypes within NX and

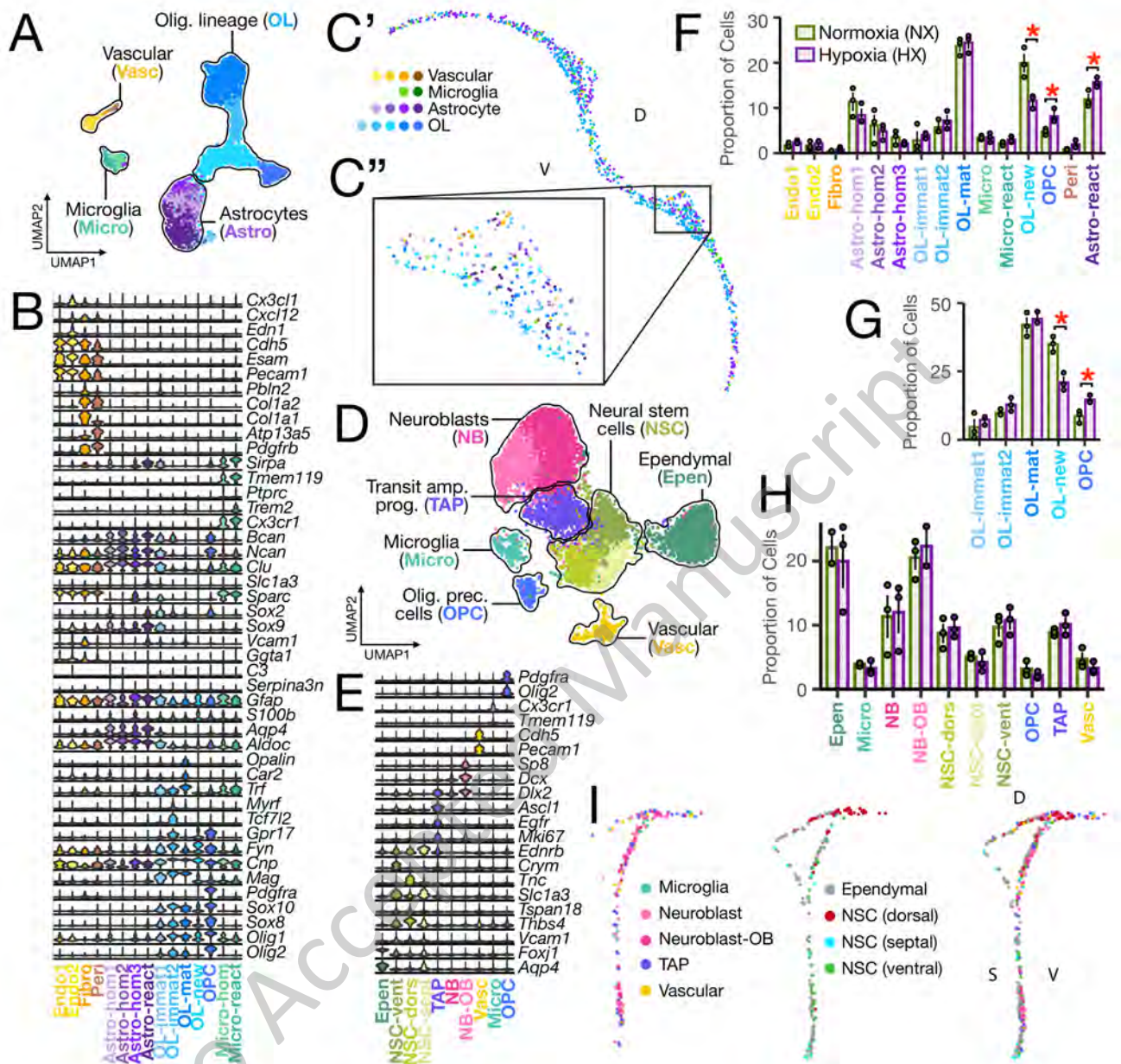
1257 HX between **(K)** corpus callosum and deep cortex, **(L)** corpus callosum and upper cortex, **(M)** upper and  
1258 deep cortex. Violin-boxplots showing astrocyte reactivity score of **(N)** all astrocytes, **(O)** homeostatic  
1259 astrocytes, and **(P)** reactive astrocytes, split and colored by condition, across the SVZ, corpus callosum,  
1260 and cortex dotplots displaying differential gene expression results of microglia reactivity genes comparing  
1261 all microglia Cell Types and Cell Subtypes within NX and HX between **(Q)** SVZ and corpus callosum,  
1262 SVZ and deep cortex, SVZ and upper cortex, **(R)** corpus callosum and deep cortex, **(S)** corpus callosum  
1263 and upper cortex, **(T)** upper cortex and deep cortex. Violin-boxplots showing microglia reactivity score of  
1264 **(U)** all microglia, **(V)** homeostatic microglia, and **(W)** reactive microglia, split and colored by condition,  
1265 across the SVZ, corpus callosum, and cortex. For all dotplots, only significant genes are shown  
1266 ( $FDR < 0.05$ ) and dot color represents average  $\log_2(FC)$  as per the associated legend. Results for all  
1267 dotplots are also shown in Extended Data Table 5-1. For all violin-boxplots, the width of the violin plot  
1268 represents the proportion of cells expressing that value of the score. Each dot represents the average  
1269 score for each replicate, the bold central line of the boxplot represents the median score for the condition,  
1270 and the limits of the box represent the interquartile range. Significance is determined using the two-tailed  
1271 Student's t-test. \*p-value  $< 0.05$ ; \*\*p-value  $< 0.01$ . Asterisks denoting p-value are colored according to  
1272 the comparison they refer to (ie. turquoise denotes comparisons of different regions within NX, purple  
1273 denotes comparisons of different regions with HX, and black denotes comparisons between HX and NX  
1274 within the same region).

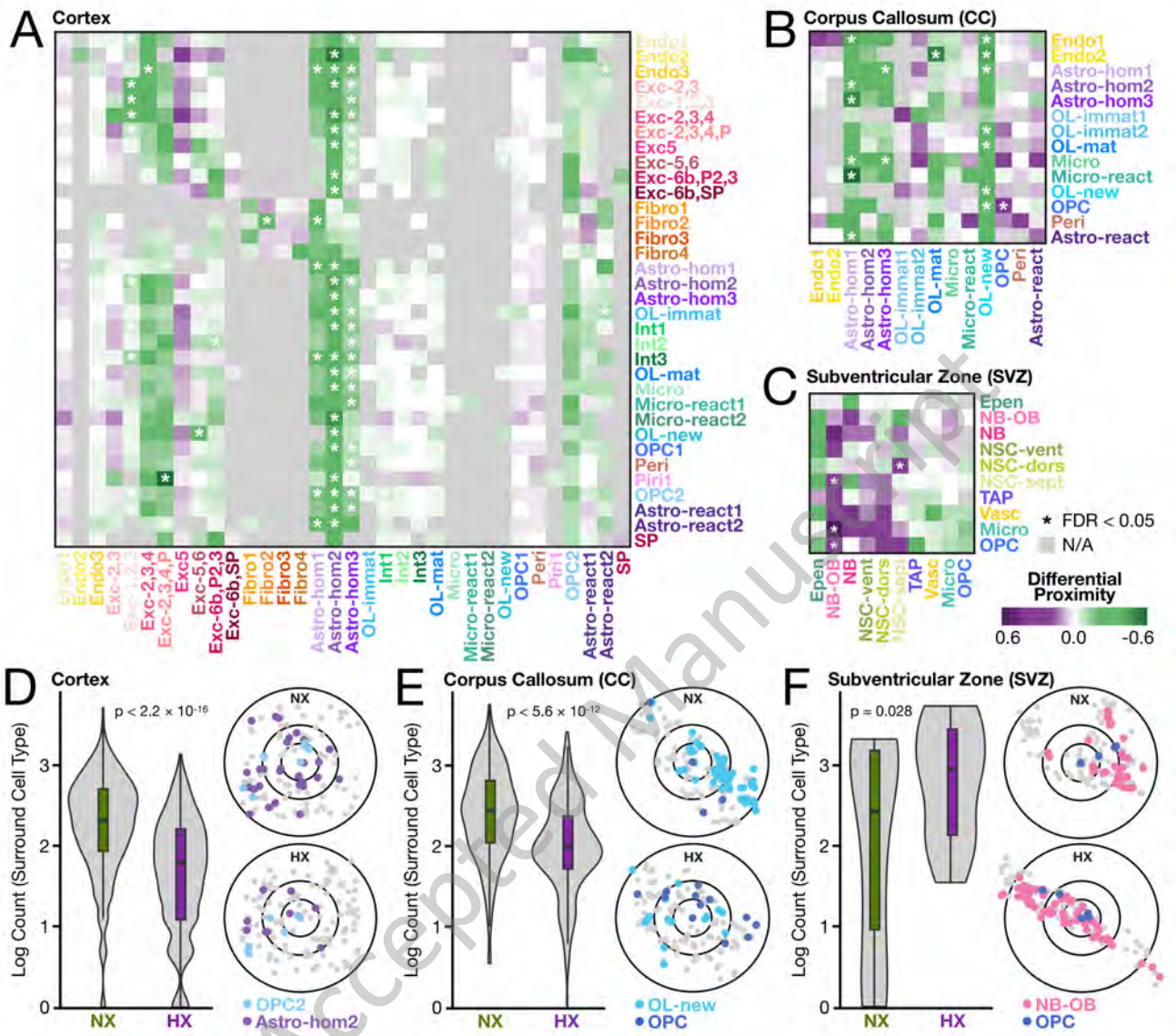
1275



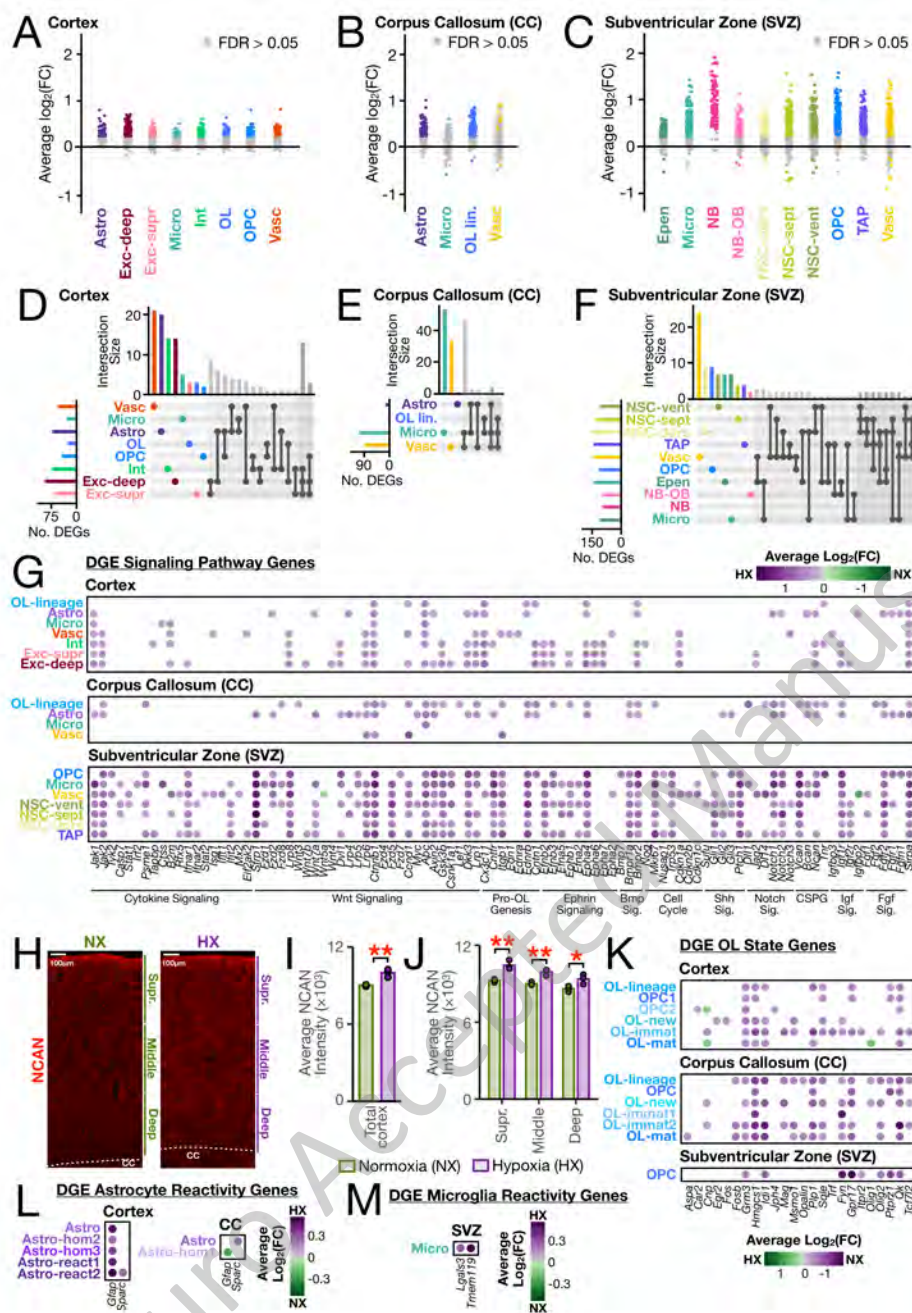




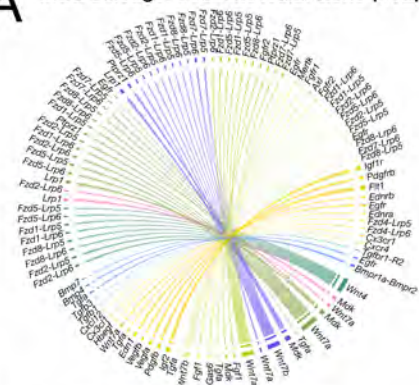




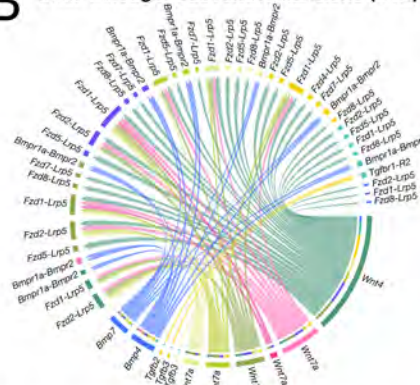




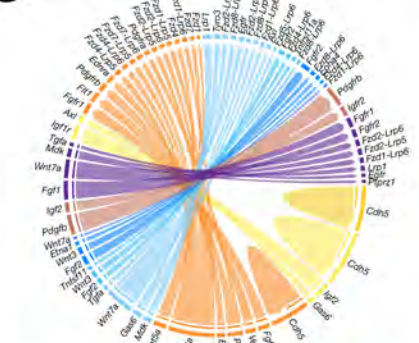
**A** Intra-Lineage: Subventricular Zone (SVZ)



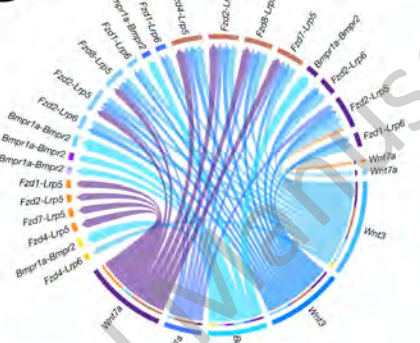
**B** Inter-Lineage: Subventricular Zone (SVZ)



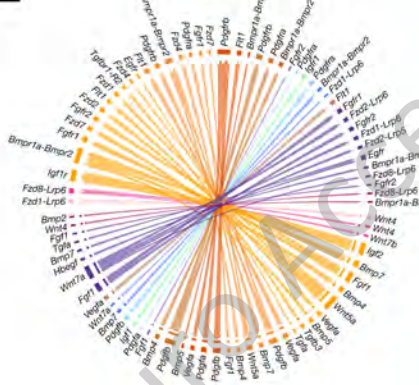
**C** Intra-Lineage: Corpus Callosum (CC)



**D** Inter-Lineage: Corpus Callosum (CC)



**E** Intra-Lineage: Cortex



**F** Inter-Lineage: Cortex

